Auditory brainstem models: K_{V1} ion-channels and depleting end-bulb synapses improve spatial encoding in reverberation

Andrew Brughera[1,2‡*], Jason Mikiel-Hunter[1‡], Mathias Dietz[3], David McAlpine[1]

[1] Department of Linguistics, and the Australian Hearing Hub, Macquarie University, Macquarie Park, New South Wales, Australia

[2] Department of Biomedical Engineering, Boston University, Boston, Massachusetts, United States of America

[3] Medizinische Physik and Cluster of Excellence "Hearing4all", Universität Oldenburg, Oldenburg, Lower Saxony, Germany

[‡] A.B. and J.M.H. contributed equally to this work.

* Corresponding author: andrew.brughera@mq.edu.au

Abstract

Listeners perceive sound-energy as originating from the direction of its source, even as the direct sound is followed only milliseconds later by reflected sound from multiple different directions. Auditory neural adaptation, before spatial information is binaurally encoded in the brainstem, is suggested as a contributing mechanism, yet the form of sufficient adaptive mechanisms remains unspecified. Though a strong preference for spatial information conveyed in early-arriving sound is observed behaviourally and neurophysiologically, investigation by simultaneously recording from binaural brainstem neurons and their monaural input neurons while controlling adaptation is yet unrealised. Therefore, here we computationally model connected neurons across the auditory brainstem, exploring two biophysical mechanisms that can account for the brainstem's emphasis of early-arriving spatial information. Matching responses in the medial superior olive (MSO), of neurons encoding interaural time differences, we demonstrate that accurate localisation in reverberant environments is enhanced by realistic pre- and post-synaptic specialisations. Short-term synaptic plasticity at the inputs from the auditory nerve to spherical bushy cells (SBCs) in the ventral cochlear nuclei that project bilaterally to the MSO, and K_{V1} membrane-channels in the SBCs and MSO neurons, promote efficient coding of spatial information, by suppressing responses to late-arriving sound, particularly at frequencies where reverberant sound is relatively intense in outdoor environments. Suiting weak reverberation outdoors at very low frequency, including 200 Hz, weak K_{V1} activity promotes accurate localisation. Applied to the lateralisation of human speech near 700 Hz in a virtual reverberant room, identical synaptic depression and strong K_{V1} activity at this higher frequency enhance correct, over spurious, localisation cues at the earliest stages of spatial processing.

Author Summary

Aurally locating a talker in a reverberant room is often challenging for hearing-impaired listeners. Sound arriving directly from the talker isn't easily distinguished from reverberant sound reflecting off walls milliseconds later. Nevertheless, normal-hearing listeners easily localize sound-sources, aurally "glimpsing" the reliable spatial information of direct sound during early, rising portions of modulated sounds, while ignoring later-arriving, confounding information corrupted by reverberation. Understanding the successful underlying mechanisms may suggest approaches to improve auditory spatial information provided to listeners with hearing aids and cochlear implants. In the auditory brainstem, binaural neurons of the medial superior olive (MSO) preferentially respond to early-arriving spatial information. As simultaneous recordings from MSO neurons and their monaural input neurons while controlling adaptation are yet unrealised, to understand the contributing mechanisms, here we identify and computationally demonstrate two suppressive brainstem mechanisms that emphasise early-arriving sound, and enhance the localisation of talkers despite reverberation: synaptic depletion in the bilateral cochlear nuclei that drive the MSO, and low-threshold potassium ion channels which support the encoding of spatial information in MSO neurons. Our models reflect the frequency-dependent behavioural emphasis of reliable, early-arriving auditory spatial information, demonstrating brain mechanisms that down-weight unreliable spatial information by spectro-temporally opposing typical outdoor reverberation.

Introduction

Sound propagating directly from its source to a listener's ears is typically followed milliseconds later by multiple reverberant copies arriving from different directions (Fig. 1). Despite this mixture of direct and reflected sound pressure generating non-stationary spatial information in the binaural cues—the interaural time difference (ITD) and interaural intensity difference (IID)—listeners typically perceive a sound as punctate, and originating from the direction of its source. Facilitating 'cocktail party listening' – attending to a single talker against a background of many competing voices – perception of the true source location can persist even when the intensity of reflected sound matches or exceeds that of the early-arriving, direct sound. (1–3)

Figure 1. Reverberant copies of direct speech produce confounding binaural cues. (A) Anechoic speech stimulus 'church', spoken at 70 dB SPL by a female talker located +30° to the right and front of listener. Spectrogram of 'dry' speech (anechoic, without reverberation) at left ear plots signal energy <1 kHz. Gammatone filters centred at 200 Hz (light grey) and 600 Hz (dark grey) used to calculate waveforms at left (blue) and right (red) ears and instantaneous ITDs (light/dark grey) for both frequencies (restricted to ±700us, human physiological range). ITDs for 'dry' speech stimulus were consistently close to +363 μs. (**B) Reverberant speech stimulus** including direct speech plus two simulated reflections from listener's left, the first from -65° delayed by 4 ms, and the second from -130° delayed by 8 ms. Reverberant copies generated increased energy at left ear (the generally brighter spectrogram, esp. in the 600-Hz channel). Additional reverberant energy also extends into the quiet gap between the vowel and second

consonant (0.45-0.55 ms), generating rapidly varying instantaneous ITDs (also restricted to ±700us), along with conflicting ILD cues especially in the 600-Hz channel.

Neural correlates of ‘echo-suppression’ are observed in the ascending auditory pathway, from auditory nerve and brainstem, to midbrain and primary auditory cortex. The brainstem emphasises early-arriving sound at both ears, as neurons of the medial superior olive (MSO) perform binaural coincidence detection. Driven bilaterally by the left and right auditory nerve via bushy cells of the ventral cochlear nuclei, MSO neurons encode spatial information through their sensitivity to ITDs conveyed in the temporal fine structure (TFS) of low-frequency (< 1500 Hz) sounds. The resulting responses of MSO neurons tuned to ITD are strongest during rising sound-energy. Adaptation in monaural projection pathways to binaural MSO neurons is believed to contribute, yet specific mechanisms for the emphasis of early-arriving direct sound in the neural pathways that support ITD-encoding remain to be identified. (4–8)

Behavioural emphasis of early-arriving ITD information is frequency dependent (9): for amplitude-modulated 600-Hz sounds, listeners are more sensitive to ITDs conveyed during the rising-energy portion than they are to ITDs at the energy peak; this is not the case at 200 Hz, where listeners are equally sensitive to ITDs conveyed during rising and peak energy, and where, in outdoor settings, reverberant energy can be 20 dB less intense at 200 Hz than at 600 Hz (10). For both frequencies, listeners are least sensitive to ITD during falling sound-energy, when direct sound is most likely to be corrupted by reverberation. These data suggest that spatial auditory brain mechanisms transmitting reliable information, and suppressing unreliable information, account for natural frequency-profiles in reverberant energy which decrease below 1500 Hz.

Here, noting the unavailability of simultaneous recordings from the MSO and cochlear nuclei with external control of adaptation, we apply a nonlinear brainstem model to explore two cooperative biophysical mechanisms for the frequency-dependent emphasis of ITD during rising and peak sound-energy: (i) short-term synaptic plasticity (synaptic depression) at the Endbulbs of Held synapses between auditory nerve fibres and spherical bushy cells (SBCs) in the ventral cochlear nuclei (11–14); and (ii) voltage-gated, low-threshold potassium (K_{V1}, K_{LT}) ion channels in MSO neurons (15–18) and in the SBCs (19) projecting bilaterally to the MSO. We test whether these biophysical features suppress responses to late-arriving sound, and support the emphasis of sensitivity to ITDs conveyed in early-arriving sound that is observed in single MSO neurons (4). Then, with our nonlinear model, and a linear spiking model (20) extended to populations of MSO neurons in the left and right brain hemispheres, we explore brainstem properties consistent with the stronger weighting of ITD information conveyed during rising energy at 600 Hz—a frequency with higher reverberant energy—compared to 200 Hz, where reverberant energy is less intrusive.

Our hemispheric MSO model then probes a possible link between relative weighting of spatial information during rising energy, and correct lateralisation of natural speech in realistic acoustic environments (the “Haas effect”) (3). We evaluate monaural synaptic depression prior to binaural interaction, in promoting correct, unambiguous judgements in the laterality of natural speech in a simulated reverberant space with direct sound and early reflections off virtual walls (4). For the 600-Hz channel investigated, achieving unambiguous, correct lateralisation would suggest a dominance of ITD information conveyed during rising sound-energy, which facilitates correct lateralisation by emphasising ITD cues of sound arriving directly from its source, over the confounding ITD cues of its reflected copies.

Results

A nonlinear brainstem model with synaptic depression and K_{V1} activity reproduces the frequency-dependent emphasis of spatial information during rising and peak sound-energy

We first explored the extent to which synaptic depression at model SBCs in the cochlear nuclei accounts for the emphasis of ITDs during the rising energy of modulated sounds in a model MSO neuron (Fig. 2B). We did so, employing amplitude-modulated binaural beats (AMBBs) (2,4), in which binaurally presented tones of a slightly different frequency are modulated in amplitude at a rate equal to the difference in frequency across the two ears. This generates a stimulus in which each cycle of rising and falling sound-energy contains a full cycle of interaural phase disparities. AMBBs (Fig. 2A) centred at 600 Hz, with modulation rates 4 to 64 Hz, were presented to a standard model of peripheral auditory processing (21,22), which drove a nonlinear model of brainstem neurons. The model of peripheral auditory processing includes 24 adapting auditory nerve fibres: twelve each in the left and right ears, with characteristic frequency (CF) 600 Hz. (CF is the frequency at which a neuron has its lowest threshold in sound pressure level, SPL, for an action potential; CF is inherited from the frequency-tuning of the inner ear, and the resulting CFs of auditory nerve fibres that distally drive a neuron.) Each of three distinct model auditory nerve fibres projects an ipsilateral, uniformly depressing (u = 0.5) (23), excitatory synaptic input to one of the eight (four left, and four right) model SBCs. Each model SBC projects a non-depressing, excitatory synaptic input to the multi-compartment model MSO neuron. The model SBCs and MSO neuron are Hodgkin & Huxley models (24), with circuit elements that represent membrane ion-channels, including K_{V1} (25–27).

Figure 2. Amplitude-modulated binaural beats (AMBBs) (2) and the nonlinear brainstem model: (A) AMBBs in which AM rate is equal to binaural-beat frequency (difference between frequencies at right and left ears). Presented via headphones, interaural phase difference (IPD) cycles through 360˚ at the same rate as AM. *Start-IPD* (the IPD at zero amplitude) is a free parameter. Shown with right-carrier 616 Hz, left-carrier 584 Hz, AM 32 Hz, and *start-IPD* 270˚ (right channel trailing by 90˚), resulting in zero IPD at the midpoint of rising-amplitude. **(B) Nonlinear brainstem model** for an MSO neuron and its excitatory inputs with synaptic depression in the cochlear nuclei. AMBBs drive a model for bilateral auditory nerve fibres (21,22) projecting individually depressing synapses (23) (u = 0.5) onto model SBCs of the cochlear nuclei (26), which in turn project bilaterally to the model MSO neuron (best-ITD = 0). The best-ITD of a neuron is the ITD of highest spike rate, typically measured with unmodulated stimuli of equal amplitude at the two ears. The nonlinear model MSO neurons of this study have best-ITDs equal to zero. **(C) Sub-compartment** in the nonlinear brainstem model (see Methods).

Beginning without synaptic depression, a nonlinear model with very strong, non-depressing, supra-threshold synapses in the cochlear nuclei, originally developed to generate strong, sustained responses (28) consistent with strong ITD sensitivity in the MSO for unmodulated pure-tone stimuli (29), produced only slight adaptation in the spike rates of its model SBCs (Fig. 3A, top row). Without synaptic depression, the model MSO neuron responded strongly to zero ITD, its best-ITD, across the amplitude modulation (AM) cycle: most strongly at peak sound-energy, slightly less strongly during rising energy, and less strongly during falling energy (Fig. 3A, lower three rows; in a 3-way comparison of spike counts for best-ITD during rising vs. peak vs. falling energy, $p < 10^{-9}$ at each modulation frequency). The slightly larger suppression

in responses to best-ITD during falling energy is supported by adaptation in the auditory nerve model, and K_{V1}-based refractory effects in the model SBCs and MSO neuron. (AMBB stimuli had increasing IPD (positive beat direction): “best-ITD during rise” denotes start-IPD = 270°; “best-ITD at peak” denotes start-IPD = 180°; and “best-ITD during fall” denotes start-IPD = 90°.)

Figure 3. AMBB cycle histograms for nonlinear model brainstem neurons acoustically stimulated by sound frequencies centred at CF **600 Hz: (A) Without synaptic depression**, auditory nerve to SBC synapses were strongly supra-threshold. Model SBCs adapted slightly. Model MSO neuron responded to best ITD strongly at peak sound-energy, and systematically less strongly during rising and falling energy (3-way comparisons, $p < 10^{-9}$). The synchrony index—a measure of temporal alignment of spikes over the AM cycle (see Methods)—ranged from 0.133 at 4 and 64 Hz to 0.161 at 16 Hz for model SBCs, and from 0.595 (64 Hz, best-ITD at peak) to 0.794 (16 Hz, best-ITD during fall) for the model MSO neuron (Rayleigh statistic, $p < 0.001$ in all cases). **(B) With synaptic depression in the cochlear nuclei**, the auditory nerve to SBC synapses were supra-threshold at full strength. Model SBCs adapted. Model MSO neuron responded to best ITD strongly during rising energy; weakly to moderately at peak; and weakly during falling, energy (3-way comparisons, $p \leq 0.003$). Synchrony-indices to AM for model SBCs ranged from 0.0485 at 4 Hz to 0.174 at 32 Hz; for model MSO neuron, from 0.450 (64 Hz, best-ITD during fall) to 0.814 (64 Hz, best-ITD during rise) (Rayleigh statistic, $p < 0.01$ for model SBCs at 4-Hz AM, otherwise $p < 0.001$). *Definitions:* Grey silhouettes: AM envelope. Black lines: static IPD functions. Best-ITD = 0. Best-ITD during rise: *start-IPD* = 270°. Best-ITD at peak: *start-IPD* = 180°. Best-ITD during fall: *start-IPD* = 90°.

188 Next, we introduced synaptic depression in supra-threshold synapses of model SBCs,
189 producing adaption in their spike rates (Fig. 3B, top row). This adaptation followed a similar
190 time-course across modulation rates, such that at low-to-moderate rates (4 to 16 Hz) most of
191 the adaptation occurred by the peak in the AM cycle, and at moderate-to-high rates (16 to 64
192 Hz) gradual adaptation is evident across much of the AM cycle. Consistent with physiological
193 and behavioural data at 600 Hz (4,9), the model MSO neuron responded to its best-ITD
194 strongly during rising amplitude, weakly to moderately (and broadly) at peak energy, and only
195 weakly during falling energy (Fig. 3B, lower three rows; in this 3-way comparison of spike
196 counts, $p \leq 0.003$ at each modulation frequency). Adapting similarly to the model SBCs, the
197 model MSO neuron had higher spike counts for best-ITD during rising energy vs. peak energy
198 at 4- to 16-Hz modulation ($p < 0.02$), and during peak vs. falling energy at 16- to 64-Hz
199 modulation ($p < 0.0025$).

200 Thus, consistent with behavioural data at the same, 600-Hz, sound frequency, a model that
201 includes synaptic depression between the auditory nerve and cochlear nuclei that drove
202 bilateral inputs to the MSO neuron, responds preferentially to ITDs during the rising energy of
203 sounds. Without this synaptic depression, the preference for spatial cues during rising sound-
204 energy is absent, suggesting a critical role for monaural input pathways to binaural neurons in
205 emphasising spatial information that is likely to be reliable in reverberant listening conditions.

206 Sensitivity to ITDs conveyed in the temporal fine structure (TFS) of sounds is subject to highly
207 specialised biophysical constraints, constraints that are generally thought to hold for sound
208 frequencies up to 1400 Hz (higher in some non-human species), covering the range over
209 which ITDs in the TFS are discriminable. Therefore, given the emphasis to ITDs during the
210 rising energy of modulated sounds at 600 Hz—concordant with perceptual and brain-imaging

data obtained at a similar frequency (2)—we might expect a similar emphasis at the lower sound-frequency of 200 Hz. Nevertheless, despite our model implementing identical biophysical elements, we observed a very different pattern of results at 200 Hz compared to 600 Hz. These differences are reminiscent of behavioural data (9): at 600 Hz, human ITD-sensitivity is strongest during rising energy with progressively less ITD sensitivity for peak and falling energy; but at 200 Hz, ITD sensitivity is strong for both peak and rising energy, and again weak for falling energy.

Employing the same model with monaural depressing synapses, identical to those which emphasised ITDs during the rising energy at 600 Hz, we assessed the relative emphasis of ITD cues in the modulation cycle of a 200-Hz AMBB stimulus for the modulation rates of 8 and 20 Hz employed by Hu et al. (9). At 200 Hz, the model SBCs showed slight adaptation in spike rate across the AM cycle (Fig. 4A, top row), less adaptation than at 600 Hz. Spike counts in the model MSO neuron (Fig. 4A, lower three rows) matched the patterns of significance in human ITD-detection for AM stimuli at 200 Hz (9): spike counts were slightly higher but not significantly for best-ITD during peak vs. rising energy, and spike counts were significantly different (higher) only for best-ITD at peak energy vs. falling energy ($p = 0.0079$ for modulation at 8 Hz; $p = 0.0014$ for modulation at 20 Hz).

Figure 4. AMBB cycle histograms for nonlinear model brainstem neurons stimulated by frequencies centred at CF **200 Hz**. Same synaptic depression and model SBCs as in Fig. 3B, adapted less at 200 Hz. **(A) Same fast model MSO neuron** as in Fig. 3B: spike counts were not significantly different for best-ITD during rising vs. peak energy, and were higher for best-ITD at peak energy vs. falling energy ($p < 0.01$). Synchrony-indices to AM for model SBCs ranged from 0.0762 at 8 Hz to 0.109 at 20 Hz; model MSO neuron from

0.433 (20 Hz, best-ITD during fall) to 0.807 (8 Hz, best-ITD during rise) (Rayleigh statistic, $p < 0.001$). **(B) Moderate-speed model MSO neuron:** spike counts were not significantly different for best-ITD during rising vs. peak energy, and were lower for best ITD during falling energy ($p < 0.005$). *Definitions:* Grey silhouettes: AM envelope. Black lines: static IPD functions. Best ITD = 0. Best-ITD during rise: *start-IPD* = 270°. Best ITD at peak: *start-IPD* = 180°. Best ITD during fall *start-IPD* = 90°. Synchrony-indices to AM for the model MSO neuron ranged from 0.825 (20 Hz, best-ITD during fall) to 0.888 (20 Hz, best-ITD during rise) (Rayleigh statistic, $p < 0.001$)

Noting recent evidence of heterogeneity in membrane speeds in the very low-frequency region of MSO (30), we applied AMBBs at 200 Hz to our nonlinear brainstem model, now modified with a moderate-speed model MSO neuron having slower dendritic and somatic membranes, derived by dividing membrane conductance values by three. The identical model SBCs again adapted less (Fig. 4B, top row) than at 600 Hz. Synaptic strength in this moderate-speed model MSO neuron was divided by two for low spike rates for best-ITD during falling energy, while retaining moderate spike rates for best-ITD during rising and peak energy (Fig. 4B, lower three rows). The moderate-speed MSO neuron then produced very few spikes at ITDs distant from best-ITD, yielding spike counts for best-ITD at peak energy that were equal to, or slightly less than, spike counts for best-ITD during rising energy. The moderate-speed model MSO neuron slightly augmented patterns of significance in human ITD-detection (9): spike counts were not significantly different for best-ITD during rising vs. peak energy, and were significantly lower for best-ITD at falling energy (8-Hz modulation: rise vs. fall, $p = 4.08 \times 10^{-05}$; peak vs. fall, $p = 0.0049$; 20-Hz modulation: rise vs. fall, $p = 1.53 \times 10^{-09}$; peak vs. fall, $p = 1.53 \times 10^{-09}$).

256 Our nonlinear brainstem model accounts for the emphasis of rising energy in ITD encoding by
257 MSO neurons at 600 Hz, and is consistent with the shift from very strong human ITD-sensitivity
258 during rising energy at 600 Hz, to strong sensitivity during both peak and rising energy at 200
259 Hz, and with weaker sensitivity during falling energy at both frequencies. As the stimulus
260 frequency is reduced from 600 to 200 Hz, the reduction in suppression at the peak of the AM
261 cycle is likely due to decreased activation of K_{V1} channels at the lower frequency, from the
262 inherently longer quiet periods between intense input spiking (31,32).

263 ***A hemispheric-difference model including synaptic depression correctly***
264 ***lateralises amplitude-modulated stimuli with temporally specific ITDs***

265 To test whether synaptic depression in combination with heterogeneous neuronal properties is
266 consistent with the behavioural observations of Hu et al. (9), we employed a neural spiking
267 model of both brain hemispheres, incorporating linear model neurons in the bilateral cochlear
268 nuclei and MSOs (20), to generate a neuro-metric measure of lateralisation. Following the
269 model concept of Dietz et al. (33), two hemispheric channels (‘left’ and ‘right’) comprised
270 distinct MSO model neuron populations (50 neurons each) whose inputs from ‘contralateral’
271 cochlear nucleus were delayed by 0.125 cycles of interaural phase difference (IPD, equal to
272 ITD x frequency) (34) such that they spiked preferentially for sounds arriving from contralateral
273 spatial locations (Fig. 5). The difference in spike rate between hemispheres, calculated (in 5-
274 ms epochs) as a signed d’, was then used as a neuro-metric measure of lateralisation (see
275 Methods) (34,35). A uniform synaptic depression (u = 0.55) (23) was implemented
276 independently at each synapse between an auditory nerve fibre and its target SBC of the
277 cochlear nucleus. Sinusoidally amplitude-modulated (SAM) tones, with non-zero, positive ITDs
278 positioned within the rising, peak, or falling phases of the AM cycle as per Hu et al. (9), and

see above, were presented to the linear model (Fig. 6). As in the behavioural study, the tone frequency (200 Hz or 600 Hz) and the AM rate (8 Hz or 20 Hz) were varied, as was the proportion (20% or 40%) of the AM cycle containing a non-zero ITD.

Figure 5. Overview of the hemispheric-difference model consisting of two MSO populations (red—left MSO and blue—right MSO), each containing fifty linear, single-compartment model neurons, with either fast or slow resonant properties (20). Each MSO neuron model receives four excitatory inputs 'bilaterally' from linear, single-compartment SBC model neurons in the CN. Four independently-simulated, individually-depressing and medium-spontaneous-rate auditory nerve fibres (21) provide excitatory drive to each SBC model neuron.

Figure 6. AM lateralisations by linear, hemispheric-difference model at 200Hz and 600Hz. (A&B) At 200 Hz, both Slow (A) and Fast (B) MSO models correctly lateralised +300 μs ITDs (top row, black) to the right (d'>1 in any 5ms bin (red vertical bands) where d' (bottom rows, black) calculated from mean spike rates of left (top rows, red) and right (top rows, blue) MSO populations) most often at peak (middle column) of 8-Hz AM cycle (top row, grey silhouettes) compared to rising (left column) and falling (right column) phases (Slow MSO: Rising, 7 bins; Peak, 12 bins; Falling, 2 bins. Fast MSO: Rising, 3 bins; Peak, 4 bins; Falling, 1 bin). Same adapting auditory nerve inputs used for both MSO neuronal types, therefore more correct lateralisations overall by Slow MSO is a result of its slower integration. **At 600 Hz (C)**, introducing +150 μs ITD (top row, black) to 8 Hz AM (top row, grey silhouettes) produced strong onset ITD sensitivity in Fast MSO towards rising phase (left column) that decreased across AM cycle (Fast MSO: Rising, 12 bins; Peak, 5 bins; Falling, 1 bin).

302 At 600 Hz, MSO neurons with fast resonant properties, i.e. akin to the nonlinear model with
303 100% K_{LT} (K_{V1}) conductance, demonstrated a strong sensitivity to the onset ITD, as indicated
304 by the increased number of instances when the AM stimulus containing a (right-leading) +150
305 μs ITD in its rising-energy phase was correctly lateralised [d' > 1 in any bin was considered a
306 correct lateralisation of a signal from the 'right' (Fig. 6 *pink vertical bands*)]. This ITD sensitivity
307 decreased across the AM cycle reaching a minimum when non-zero ITDs were restricted to
308 the falling-energy phase (Fig. 6 *bottom row*). The trend for onset dominance at 600 Hz was
309 true for both modulation rates (8 Hz and 20 Hz) and when the proportion of the AM cycle
310 containing non-zero ITDs was either 20% or 40% (Fig. 7 *right column*). Notably, in all three
311 portions of the AM cycle, the number of correct lateralisations decreased as the proportion of
312 an AM cycle containing a non-zero ITD was decreased from 40% to 20% (Fig. 7 *right column*,
313 blue).

314 **Figure 7. Summarising correct lateralisations of SAM stimuli by the hemispheric-**
315 **difference model.** Mean (±SEM) time correctly lateralised per presentation (number of
316 correct lateralisations * bin duration / 25 presentations) by either Slow MSO neurons at
317 200 Hz (left column) or Fast MSO neurons at 200 Hz and 600 Hz (middle and right
318 columns respectively). Modulation rates of 8 Hz (top row) and 20 Hz (bottom row) were
319 tested. ITDs were inserted into either 20% (blue dotted) or 40% (black solid) of the AM
320 cycle during Rising, Peak, or Falling energy. At 600 Hz, the Fast MSO displays dominant
321 ITD weighting at onset that decreased significantly across AM cycle (Two-way ANOVA,
322 interaction of AM cycle phase x Percentage ITD insertion: 8-Hz AM, $F(2,48) = 8.310$, $p =$
323 0.001; 20-Hz AM, $F(2,48) = 50.098$, $p = 0.0001$). At 200 Hz, the Fast MSO showed equal
324 or better ITD sensitivity at Peak compared to Rising energy (Two-way ANOVA, interaction

of AM cycle phase x Percentage ITD insertion: 8-Hz AM, $F(2,48) = 7.83$, $p = 0.001$; 20-Hz AM, $F(2,48) = 36.01$, $p = 0.0001$). Slow MSO generated more correct lateralisations than Fast MSO (Two-way ANOVA, interaction of AM cycle phase x Neuron Type: 8-Hz AM, $F(2,48) = 18.82$, $p = 0.0001$; 20-Hz AM, $F(2,48) = 13.12$, $p = 0.0001$) with equal or augmented ITD sensitivity at Peak for 40% non-zero ITD (Paired two-tailed T-test, Mean Peak – Rising, N = 25: 8-Hz AM, $t(24) = 2.21$, $p = 0.037$; 20-Hz AM, $t(24) = 2.21$, $p = 2.37 \times 10^{-4}$). Correct lateralisations also increased as the percentage of AM phase containing non-zero ITD was raised from 20% to 40% (Three-way ANOVA, main effect of Percentage ITD insertion: Fast MSO, $F(1,24) = 418.78$, $p = 0.0001$; Slow MSO, $F(1,24) = 285.622$, $p = 0.0001$)

When an amplitude-modulated 200-Hz tone (with a right-leading, non-zero ITD of +300 μs) was presented to the fast MSO model, the onset dominance observed at 600 Hz was replaced by an increased weighting of ITD cues towards the peak of the AM cycle (Fig. 6). Indeed, the frequency of correct lateralisations at the peak of AM cycles was either equal to (8-Hz AM stimuli) or higher (20-Hz AM stimuli) than that observed at corresponding onset phases (Fig. 7 *middle column*). As at 600 Hz, reducing the proportion of the AM cycle containing a non-zero ITD from 40% to 20% also generated fewer correct lateralisations across all AM phases (Fig. 7 *middle column*, blue). Whilst the fast-resonant MSO model could reproduce behavioural trends observed by Hu et al. (9) at both carrier frequencies, it generated fewer correct lateralisations overall at 200 Hz (Fig. 7 *middle* and *right columns*). We therefore presented the same 200-Hz carrier stimulus to the linear model MSO neurons with slower, less resonant membrane properties (Fig. 6). This generated a higher number of correct lateralisations overall, while

347 maintaining, or even augmenting, the maximum weighting of ITD at the peak AM energy in all
348 conditions tested (Fig. 7 *left column*).

349 Our linear model, therefore, suggests that a slower, more integrative MSO neuron may assist
350 lateralisation in lower-frequency channels, in particular by extending the extraction of ITD
351 information towards peak energy in the AM cycle, where human ITD detection is best when
352 comparing at 200 Hz across the AM cycle (9). Additionally, our model qualitatively matched the
353 behavioural data by demonstrating a higher propensity to lateralise stimuli of either frequency
354 when 40% vs. 20% of the AM cycle contained a non-zero ITD.

355 *Synaptic depression improves the hemispheric-difference model's ability*
356 *to lateralise speech in artificial reverberation*

357 If neural adaptation prior to binaural integration contributes to accurate source localisation, we
358 would expect it to aid lateralisation of speech in a reverberant room, by emphasising ITD cues
359 associated with direct sound over reverberation (Fig. 1 *far left*) (4). Speech signals were
360 presented to the neural model of lateralisation under simulated anechoic (non-reverberant) and
361 reverberant conditions. We then observed whether the model correctly lateralised the side to
362 which the source was located in the presence or absence of synaptic depression in SBCs of
363 the cochlear nuclei.

364 In the anechoic condition (Fig. 8A), a word token ('church') was presented to the non-adapting
365 linear model from a virtual location 1 metre away from the target and 30 degrees to the right of
366 the midline. The speech waveform—gammatone-filtered at 600 Hz (Fig. 8A *top row*)—was
367 more intense at the right ear (red), and led the left-ear signal (blue) by an average ITD of +363
368 μs (Fig. 8A *top row*, dark grey). This generated a larger response from model neurons in the

369 ‘left’ MSO (Fig. 8A *middle row*) and multiple bins throughout the speech token where d’ values
370 were > 1 (Fig. 8A *pink vertical bands*), indicating that the talker was correctly lateralised to the
371 right in the non-adapting, linear model.

372 **Figure 8. Lateralisation of ‘anechoic’ and ‘reverberant’ speech stimuli by the**
373 **hemispheric-difference model (fast MSO, 600-Hz channel) with and without**
374 **synaptically adapting inputs from the auditory nerve to the cochlear nucleus: (A)**
375 **Anechoic stimulus** is correctly lateralised to the right (pink vertical bands) for long periods
376 independently of non-adapting (left column) or adapting (right column) synaptic inputs. Dry
377 speech stimulus gammatone-filtered at 600 Hz with instantaneous ITDs (top row), mean
378 firing rates of left (middle row, red) and right (middle row, blue) MSOs and d’ neuro-metric
379 (bottom row) are displayed. **(B) Reverberant stimulus** requires adapting synaptic inputs
380 (right column) for correct lateralisations alone (pink vertical bands). Non-adapting synaptic
381 inputs to the cochear nuclei produced both correct (left column, pink vertical bands) and
382 incorrect lateralisations (left column, light blue vertical bands) due to reverberant stimulus’
383 highly variable ITDs and confounding ILDs (top row). The inclusion of synaptic depression
384 from the auditory nerve to the cochlear nuclei (using the same auditory nerve simulations)
385 removes all incorrect lateralisations. Remaining correct lateralisations correspond with
386 stimulus onsets (right column, pink vertical bands). **(C) Quantifying incorrect**
387 **lateralisations with non-adapting and adapting synaptic inputs** (same auditory nerve
388 simulations for both) over a hundred presentations of the reverberant speech stimulus.
389 Synaptic depression produces a five-fold decrease in incorrect lateralisations ($N = 100$,
390 $t(99) = 9.51$, $p = 1.31 \times 10^{-15}$, two-tailed paired T-test).

In the reverberant condition, the same word token was presented to the non-adapting linear model from the same angle and distance, however it was also followed by two delayed copies generated by early reflections off virtual walls added behind, and to the left of, the listener (Fig. 1B *far left*). This mixture of sound arriving direct from the source and early reflective copies led to a more complex waveform (including a more intense signal at the 'left ear' (direct-to-reverberant ratio: -4dB; mean ILD: -3 dB)) whose running ITDs fluctuated between extremely large positive and negative values, culminating in an average ITD of +711 μs, a value outside the human physiological range. Although the resulting d' output exceeded 1 in eleven epochs coinciding with waveform onsets (Fig. 8B, *left*, *pink vertical bands*), it was also briefly lower than -1 in the opposite direction during three intermediate epochs (Fig. 8B, *left*, *blue vertical bands*), indicating a potentially ambiguous left-right localisation output.

We then increased adaptation by introducing synaptic depression to the monaurally driven inputs from auditory nerve fibres to the cochlear nuclei of the linear model, and presented the same reverberant stimulus (Fig. 8B) as in the previous condition. Despite the potentially confounding ITD (and ILD) cues (Fig. 8B *top row*), adding adaptation in the monaural input pathways enhanced the performance of the binaural model MSO neurons, and generated correct lateralisations of the true source to the right: the d' output exceeding 1 in six time bins without ever crossing below -1 (Fig. 8B *bottom row, right*). When the number of incorrect lateralisations was tallied over a hundred presentations of the reverberant stimulus (Fig. 8C), incorrect lateralisations were observed five times less frequently when synaptically depressing auditory nerve inputs were included in the linear model (mean incorrectly lateralised time for non-depressing synaptic inputs = 6.75 ± 0.50 ms/presentation vs. mean incorrectly lateralised time for depressing synaptic inputs = 1.3 ± 0.24 ms/presentation). This neuro-metric profile

414 agrees with the psychoacoustic percept as has been previously described for similar word
415 tokens (4), suggesting that synaptic adaptation helps to lateralise ethological sounds in
416 reverberant environments.

417 Discussion

418 *The brainstem suppresses responses to late-arriving reverberant sound in*
419 *neural pathways that encode spatial cues*

420 The ability to localise the source of a sound in reverberant environments, where reflections
421 from acoustically opaque surfaces can degrade the accuracy of auditory spatial cues, is critical
422 to prey and predator alike, and important for communication in human listeners. To explore the
423 contribution of the brainstem to sound source localisation, noting the unavailability of
424 simultaneous recordings from the MSO and cochlear nuclei with external control of adaptation,
425 we here apply physiologically realistic models of connected neurons across the auditory
426 brainstem. We find that accurate localisation in reverberation is enhanced by both synaptic
427 depression at spherical bushy cells (SBCs) in the ventral cochlear nucleus that project
428 bilaterally to the medial superior olive (MSO, a site of primary binaural integration)—as well as
429 by K_{V1} channels in the cochlear nuclei and the MSO that activate more strongly at relatively
430 higher sound-frequencies. We show that these mechanisms account for the observed ability of
431 MSO neurons to respond preferentially to ITDs conveyed during the early, rising-energy
432 portion of low-frequency sounds near 600 Hz (4). Reflecting the perception of normal-hearing
433 listeners at 500 Hz (2), our models successfully glimpsed the ITD cues conveyed in the
434 temporal fine structure during the rising portion of the AM cycle, suppressing spatial
435 information conveyed in all later portions of the AM cycle, including the portion with highest

energy. Whilst relatively weak synaptic depression in the MSO may also contribute, preliminary modelling without synaptic depression in the cochlear nuclei showed that stronger synaptic depression in the MSO disrupted ITD sensitivity without sufficiently emphasising early-arriving spatial information.

Suppression by K_{V1} channels opposes typical frequency-profiles of reverberant energy in natural outdoor scenes

K_{V1} channels are known to enhance synchrony to sound in bushy cells of the anteroventral cochlear nuclei (28), and support ITD sensitivity in the MSO (15). Our results suggest that K_{V1} channels also underlie the frequency dependence of ITD detection performance, observed behaviourally when ITDs are applied to different segments of the AM cycle (9). Intrinsic K_{V1}-channel properties, that decrease K_{V1} activation more during the longer quiet periods that occur between periodic bursts of intense input spiking at lower stimulus frequencies (31,32), are likely contributing mechanisms for the shift from very strong human ITD-sensitivity during rising energy at 600 Hz, to strong sensitivity during both peak and rising energy at 200 Hz, with weaker sensitivity at both frequencies during falling energy when direct sound for accurate source localisation is most likely to be corrupted by reflected sound.

Natural outdoor acoustics appear to have influenced brain mechanisms that suppress responses to reverberation. In many outdoor environments, including rural forests and fields, and urban streets, reverberation-time ('T60'—the time for reverberant energy to fall by 60 decibels) decreases as sound frequency decreases below 1500 Hz (10). As reverberation times decrease to a minimum near 200 Hz, K_{V1} activity independently decreases (31,32), yet remains highly effective in suppressing late-arriving sound at 500-600 Hz, with this suppression notably decreasing by 200 Hz. To the extent that spike rates of auditory nerve

459 fibres decrease with lower sound-frequency, synaptic depression at neurons in the cochlear
460 nuclei may also decrease. At very low frequencies, including 200 Hz, where reverberant
461 energy in natural, outdoor scenes is low, suppression of spatial information during peak energy
462 is less important. However, in modern, indoor listening environments, characterised by
463 enclosures with highly reflective walls, reverberation can be high even at very low frequencies.
464 Indoor reverberation combined with weakly suppressing neurons, and with increasing
465 perceptual thresholds for ITD at sound frequencies below 500 Hz (36), may contribute to the
466 observed low perceptual weighting of very low frequencies when localising broadband sound
467 (37). This consistent perceptual down-weighting for localisation, presumably by brain centres
468 above the brainstem, occurs even as these very low sound frequencies contain and apparently
469 convey vital speech information, including the fundamental frequency, and first formant of
470 vowels.

471 Contrasting the relatively weak reverberation and weak suppression of late-arriving sound at
472 200 Hz, with the relatively strong suppression at 600 Hz and increasing reverberation with
473 higher sound frequency up to 1500 Hz, suggests that brainstem neurons effectively suppress
474 responses to reverberation for sound frequencies from 500 to 1200 Hz, a frequency range that
475 despite being relatively high in reverberation produces the lowest perceptual thresholds for ITD
476 discrimination in human listeners (36,38), and dominates the percept of auditory spatial cues
477 (37,39,40).

478 MSO neurons tuned to very low sound-frequencies, though remaining faster than other types
479 of neurons, nonetheless include a range of membrane time-constants (30). By not expressing
480 more ion channels than required, the slower MSO neurons encode ITD efficiently, realising a
481 cellular energetic advantage. Consistent with the reported heterogeneity in temporal

482 properties, both moderate and fast nonlinear model MSO neurons reflected human ITD
483 sensitivity at 200 Hz (9). Reduced, but still viable, K_{V1} activity provided ITD sensitivity at 200
484 Hz in the nonlinear model, while combining with synaptic depression in the cochlear nuclei to
485 suppress responses during falling energy. Introducing slower membranes in linear model MSO
486 neurons boosted the hemispheric-difference model's ability to lateralise 200-Hz signals,
487 especially at their energetic peak, suggesting a functional benefit to a reduced density of K_{V1}
488 channels at lower frequencies.

489 Within the input pathways to the MSO, compared with the strong synaptic depression
490 observed *in vitro* (11–14), the contrastingly weak synaptic depression reported *in vivo* (41,42)
491 may indicate heterogeneity. In the excitatory pathway, weakly depressing synapses may
492 innervate and explain the subpopulations of spherical bushy cells with strong sustained
493 responses, both primary-like (43) and high-synchrony (28). Inputs to the MSO driven by these
494 weakly adapting neurons would account for MSO neurons with strong sustained responses
495 (29), which may contribute to listeners' ability to locate slowly moving sources of sustained
496 sounds.

497 Whilst inhibition including GABAergic forms is linked to enhanced membrane excitability and
498 added precision in ITD encoding (17,44,45), our results suggest that synaptic depression and
499 intrinsic membrane properties, combined with excitatory binaural coincidence detection
500 mechanisms, fundamentally contribute to perceived location based on ITD. The success of our
501 simplified, purely excitatory, input model is consistent with the view that inhibition to MSO
502 neurons does not produce strongly adaptive effects, and that the glycinergic inhibition is
503 reasonably fast-acting, largely contralaterally driven and leads contralateral excitation in time—

504 with the main effect that best-ITD is shifted toward contralateral-leading ITDs by delaying the
505 net excitatory post-synaptic current generated by the contralateral ear (46,47).

506 ***Synaptic adaption enhances correct lateralisation of reverberant speech***

507 Early reflections—those following the direct signal by 50 ms or less (48)—can disrupt low-
508 frequency sound localisation in realistic auditory environments by conveying spurious ITD cues
509 in the TFS of sounds (49). Despite this, normal-hearing listeners are highly adept at locating
510 the true source of a sound in reverberant environments including speech in reverberant
511 environments. By demonstrating that the addition of synaptic adaption to a hemispheric 2-
512 channel model emphasises ITD cues in sound onsets, our data suggest one means by which
513 complex sounds, including speech, are reliably lateralised.

514 Whilst our adapting hemispheric-difference model correctly lateralised reverberant speech, this
515 was based on its d' output surpassing a threshold value in only six of the ninety 5-ms bins
516 where a correct ITD cue was available. Nevertheless, although this neuro-metric measure may
517 not appear particularly robust, it should be remembered that only the 600-Hz frequency
518 channel was examined for the lateralisation of speech. Studies of the precedent effect—the
519 suppression of auditory information, including spatial information—for late-arriving sounds—
520 and localisation in reverberant conditions have demonstrated strong weighting of cues in the
521 500-750 Hz frequency range (37,39,40), but they also highlight the inability of subjects to
522 localise pure tones in echoic conditions, suggesting that enhanced localisation of speech in
523 reverberant conditions involves localisation cues across the low-frequency spectrum. Adding a
524 midbrain stage where neurons in the inferior colliculus (IC), for example, receive inputs from
525 MSO neurons across a wide range of CFs would further test the extent to which synaptic

526 adaptation in the cochlear nuclei improves the localisation of speech in reverberant
527 environments.

528 We note that onset-cue dominance is demonstrated extensively in the precedence effect
529 (50,51), where suppression of neural responses to a brief lagging stimulus occurs over a range
530 of delays between leading and lagging stimuli. A future localisation model combining monaural
531 synaptic depression, potentially with inhibitory echo-suppressive mechanisms, such as
532 delayed inhibition to the midbrain (52–54), and feedforward inhibition in the brainstem from
533 dorsal to ventral cochlear nucleus (55) and from ventral cochlear nucleus to MSO via the
534 trapezoid body (56–58), would provide one means of exploring whether these mechanisms act
535 cooperatively in robust onset-ITD processing in reverberant conditions. The inhibition from
536 dorsal to ventral cochlear nucleus is associated with non-monotonic rate-level functions in
537 SBCs, and not with adaptation. This inhibition has onset dynamics that are too fast to account
538 for the slower adaptive suppression of brainstem responses to late-arriving sound (4). The
539 omission of this inhibition in our models explains why the model excitatory synapses in the
540 cochlear nuclei are slightly weaker than expected. More broadly, brainstem and midbrain
541 mechanisms may combine additively or act independently for different stimuli. At least for
542 ongoing, amplitude-modulated sounds, the emphasis early-arriving sound in ITD-encoding by
543 MSO neurons, combined with the lack an increase in this emphasis at the inferior colliculus of
544 the midbrain (4), suggests that the brainstem contributes significantly to accurate sound
545 localisation in reverberation.

546 *Early-arriving spatial cues for bilateral cochlear implant (bCI) listeners*

547 To help bCI listeners receive spatial information, bCI processors can deliver enhanced spatial
548 information that emphasises sound sources over reverberation. Such enhanced spatial

information might be added to a recently developed bilateral stimulation technique that provide detectable ITD in high-rate pulse trains by including bursts of even more rapidly successive pulses (59). High-rate pulse trains with amplitude driven by sound are applied for speech intelligibility. The bursts occur at a low rate, and their contained rapid succession of current pulses within each ear overcome the excessive adaptation that can greatly reduce responses to ITD in bCI listeners (60,61). Although bCI listeners are most sensitive to ITD during peaks in sound-energy (9), acoustically the most accurate ITD-information for source location may still occur during rising sound-energy (2). To maximise ITD sensitivity, and provide spatial information that emphasises sound sources, bCI processors can during peak energy provide pulse bursts with spatial information derived earlier from the interaural cues soon after the preceding energy minimum. Calculation of interaural cues might be triggered by time since a detected energy minimum, and proportional energy increase.

Conclusions

Suppressive biophysical mechanisms producing adaptation in the auditory brainstem contribute to sound-source localisation, by promoting reliable spatial encoding despite reverberation. The frequency-dependent emphasis of auditory spatial information conveyed in early-arriving sound is consistent with brain mechanisms that transmit reliable information, and suppress unreliable information. As the brainstem encodes interaural time differences for determining sound-source locations, its suppression of late-arriving spatial information, by short-term synaptic plasticity and K_{V1} channel activity, promotes accuracy and accounts for typical frequency-profiles of reverberant energy in natural outdoor scenes.

Methods

Nonlinear brainstem model

This computational model (Fig. 2B) incorporates an MSO neuron and its excitatory input pathways including synaptic depression in the cochlear nuclei. Amplitude-modulated binaural beats (AMBBs) at 75 dB SPL rms at peak amplitude were applied as acoustic stimuli to the Zilany et al. auditory periphery model for humans (21,22) implemented in Matlab (www.mathworks.com), including 12 left and 12 right model adapting auditory nerve fibres of medium spontaneous rate, which project to depressing synaptic inputs on model SBCs in the ventral cochlear nuclei (23,26). Three model auditory nerve fibres drive each model SBC. Four left and four right SBCs project non-depressing, excitatory synaptic inputs to a multi-compartment model MSO neuron (36) with recent updates. These model brainstem neurons are implemented as Hodgkin & Huxley models (24) in the Python 3.7 Brian2 Neural Simulator (62).

Model SBCs with synaptic depression

Spherical busy cells (SBCs) are modelled as point neurons (26), Type II compartment, adjusted for temperature 37°C) with three independent, excitatory synapses each driven by a model auditory nerve fibre. Each model synapse is an excitatory synaptic conductance in series with an excitatory reversal potential of 0 mV. Each input spike causes a variable increment in its synapse's excitatory conductance which decays exponentially with time constant 0.2 ms. The increment (i.e., the synaptic strength) is variable due to synaptic depression. Synaptic depression at the individual synapses is modelled as in Rudnicki and Hemmert (23): immediately after an input spike and its associated increment in excitatory

592 conductance, the synaptic strength is multiplied by 1 – *u,* where *u* = 0.5, comparable to
593 measurements *in vitro* (11–13). This synaptic depression recovers with a single-exponential
594 function with time constant 25 ms (12).

595 Modelled synaptic depression contributed to realistic responses to AMBB stimuli, consistent
596 with low synchrony to AM in the auditory nerve at high SPL (63), and reduced synchrony in
597 primary-like neurons (including bushy cells) of the cochlear nuclei (64). Compared with a single
598 input, three inputs per model SBC (65) increased spike rates, further reduced synchrony to
599 AM, and supported a realistically small number of excitatory inputs (66) to the model MSO
600 neuron.

601 *Model MSO neuron*

602 The model MSO neuron has separate compartments representing the bilateral dendrites,
603 soma, and axon of the neuron (67). The soma is spherical and iso-potential. Best-ITD and
604 best-IPD are zero. Parameters for each compartment (Table 1) are explained below. Certain
605 parameters (Table 2) were adjusted for the four conditions yielding results shown in Figs. 3-4.

Table 1. Model MSO neuron parameters with membrane conductance at full value

Parameter	Dendrites (2)	Soma (spherical)	Axon
Temperature (˚C)	37	37	37
Number of sub-compartments	20	2	51
Diameter (μm)	3.5	30	2
Length (μm)	150	30	400
Resistivity, R_S (ohm x cm)	150	0 (iso-potential)	150
C_M (μF/cm^2)	1	1	1
V_{KLT} (mV)	-106	-106	-106
V_{Na} (mV)	n/a	-62.1	-62.1
V_H (mV)	-43	-43	-43
V_L (mV)	-60	-60	-65
$gmax_{KLT}$ (S/cm^2)	0.00132	0.0324	0.0595
$gmax_{Na}$ (S/cm^2)	0 (none)	0.0432	0.25
$gmax_H$ (S/cm^2)	0.00066	0.0216	0.0025
g_L (S/cm^2)	0.00005	0.00005	0.00005
V_E (mV)	0	n/a	n/a
$V_{AP\text{-}THRESHOLD}$ (mV, set)	n/a	n/a	-20
V_{REST} (mV)	-60.53	-60.52	-64.35

Table 2. Each column gives parameter values for one of the four cases explored. Adjusted parameters were CF, synaptic strength and synaptic depression of inputs to SBCs, membrane conductance in MSO soma and dendrites, and MSO synaptic strength:

Results shown in	Fig. 3A	Fig. 3B	Fig. 4A	Fig. 4B
CF (Hz)	600	600	200	200
Model SBC excitatory synaptic parameters:				
Full Synaptic Strength, Δg_E (nS)	400	83	83	83
Synaptic Time Constant, τ_E (ms)	0.2	0.2	0.2	0.2
Depression, u	0 (none)	0.5	0.5	0.5
Recovery Time Constant (ms)	n/a	25	25	25
Model MSO membrane conductance factor and excitatory synaptic parameters:				
$g_{MEMBRANE}$ Factor	1	1	1	1/3
Membrane Time Constant (ms)	0.33	0.33	0.33	1.0
Synaptic Strength, Δg_E (nS)	21	36	36	18
Synaptic Time Constant, τ_E (ms)	0.4	0.4	0.4	0.4

Eight excitatory synapses are located on the model MSO bilateral dendritic membranes, one each at 42.5, 47.5, 52.5, and 57.5% of the dendritic length. Each synapse is modelled as a variable conductance (g_E) in series with an excitatory reversal potential (V_E) of 0 mV. The synapses are non-depressing, and each is driven by a single model SBC from the same side. An input spike increments its synaptic conductance by a fixed amount, and the conductance then decays exponentially with time constant 0.4 ms. Synaptic strength (Δg_E), which is the fixed conductance-increment, was adjusted according to CF, the overall membrane conductance including g_{KLT}, and the presence or absence of synaptic depression in the cochlear nuclei.

Within the model MSO neuron, its functional electric-circuit unit the sub-compartment (Fig. 2C) connects to its neighbouring sub-compartments via series resistivity (R_S) representing the neuron's internal cytoplasm. Within each sub-compartment, the neural membrane is modelled as a transmembrane capacitance (C_M) in parallel with ion-channel populations: sodium ion (Na^+) channels, hyperpolarisation-activated cyclic nucleotide (HCN, I_h) channels for non-specific cations, and K_{LT} (K_{V1}) channels. Each ion-channel population is represented as a reversal potential (V_{Na}, V_H, V_{KLT}) in series with a conductance (g_{Na}, g_H, g_{KLT}). With the exception of a fixed leakage conductance (g_L) representing voltage-insensitive ion channels, each conductance value is equal to a maximum conductance multiplied by voltage-sensitive activation and inactivation gating variables with integer exponents (24).

Kirchhoff's current equation, applied to the model MSO neuron, states that the sum of the membrane and series currents exiting any point in the model neuron is zero:

$$0 = i_{C_M} + i_{Na} + i_{K_{LT}} + i_H + i_L + i_{S1} + i_{S2}$$

Series currents, i_{S1} and i_{S2}, are calculated by the Brian2 simulator according to the voltage differences, resistivity, and geometry of the related sub-compartments.

Capacitive membrane current (i_{C_M}) increases with membrane capacitance and the time-derivative of membrane potential *V*:

$$i_{C_M} = C_M \frac{dV}{dt}.$$

Leakage current: $i_L = g_L(V - V_L)$.

Sodium current (27): $i_{Na} = g_{Na}(V - V_{Na})$.

Na^+ conductance: $g_{Na} = gmax_{Na} m^4 (0.993h + 0.007)$.

Each voltage-sensitive ionic conductance has a constant maximum conductance value ($gmax$) (Table 1), and has voltage and time dependencies defined by a subset of the activation/inactivation variables m, h, w, z, and r, each with a rate of change governed by a first-order differential equation with a time constant divided by the Q_{10} temperature factor of $3^{(T-22)/10}$, where *T* is set equal to human body temperature, 37°C. For sodium:

$$\frac{dm}{dt} = Q_{10}(m_\infty - m)/\tau_m$$

$$\frac{dh}{dt} = Q_{10}(h_\infty - h)/\tau_h$$

For model Na^+ channels, steady-state activation (m_∞) and inactivation (h_∞), and their respective time constants (τ_m and τ_h) in milliseconds, are functions of membrane potential in millivolts, equal to those in Scott et al. (27):

$$m_\infty = 1./(1 + \exp((V + 46.) / (-11.)))$$

$$\tau_m = ((0.141 + (-0.0826 / (1 + \exp((-20.5 - V) / 10.8)))) / 3.)$$

$$h_\infty = 1./(1 + \exp((V + 62.5) / 7.77))$$

$$\tau_h = ((4. + (-3.74 / (1 + \exp((-40.6 - V) / 5.05)))) / 3.)$$

K_{LT} current (15):

$$i_{KLT} = g_{KLT}(V - V_{KLT}).$$

$$g_{KLT} = gmax_{KLT} w^4 z.$$

$$\frac{dw}{dt} = Q_{10}(w_\infty - w)/\tau_w$$

$$\frac{dz}{dt} = Q_{10}(z_\infty - z)/\tau_z$$

$$w_\infty = 1./(1 + \exp((V + 57.34)/(-11.7)))$$

$$\tau_w = ((21.5/((6.* \exp((V + 60.)/7.)) + (24.* \exp(-1 * (V + 60.)/50.6)))) + 0.35)$$

$$k = 0.27$$

$$z_\infty = ((1. - k)/(1 + \exp((\mathrm{V} + 67.)/6.16))) + k$$

$$\tau_z = ((170./(5.* \exp((V + 60.)/10.) + \exp((V + 70.)/8.))) + 10.7)$$

Non-inactivating HCN current (26):

$$i_H = g_H(V - V_H).$$

$$g_H = gmax_H r\ .$$

$$\frac{dr}{dt} = Q_{10}(r_\infty - r)/\tau_r$$

$$r_\infty = 1./\,(1 + \exp((\mathrm{V} + 76.)\,/\,7.))$$

$$\tau_r = ((100000./\,(237.*\exp((\mathrm{V} + 60.)\,/\,12.) + 17.*\exp(-(\mathrm{V} + 60.)\,/\,14.))) + 25.)\,.$$

Approach for setting maximum conductance values of MSO ion-channels

By selecting equilibrium membrane potentials (V_{REST}) and equilibrium ratios of i_{Na} to i_H to i_{KLT} in each compartment (0:1:-1 in dendrites; 1:4:-5 in soma, 1:1:-2 in axon), and knowing C_M and membrane time constants, the current equation yielded a maximum conductance value for each ion-channel in each compartment that produced: K_{LT} activation in dendrites and soma; Na^+ inactivation in soma; Na^+ not inactivated in axon.

Model MSO membrane time constants

In the resulting model MSO neuron of this study, with bias current to centre the somatic membrane potential at -57.6 mV, slightly above V_{REST}, the somatic membrane impedance magnitude as a function of frequency was lowpass with a resonance at 480 Hz. Although this resonance frequency is slightly higher than typical for MSO neurons (20,68), this 480-Hz resonance frequency multiplied by 2π converts to an angular frequency of 3016 radians/s, with its reciprocal yielding a membrane time constant of 0.33 ms that is within the range of MSO neurons (69). For AMBB stimulation centred at 200 Hz, to reflect the range of MSO membrane speeds at very low CF (30), slower somatic and dendritic membranes were also modelled by dividing the fast membrane conductances by three to yield a somatic membrane time constant of approximately 1 ms.

AMBB period histograms

For each AMBB period histogram from the nonlinear model, spikes were counted in forty non-overlapping bins, each covering 1/40 of the AM cycle. Histograms showing results from the

nonlinear model were not smoothed. Spike rates were calculated by dividing the spike count by the total time duration for each bin, across the multiple periods of eight different stimulus presentations of 0.75-second duration.

Eight starting-phases at decrements of 45° efficiently implemented IPDs

At each carrier and modulation-frequency combination, 8 acoustic stimuli, each with 1 of 8 carrier *starting-phases* (0°, -45°, -90°, …, -315°), were applied at each model ear, driving auditory nerve fibres. For computational efficiency, *start-IPD* (the IPD at zero amplitude) was achieved by pairing spike times from each *starting-phase* in one ear, with the spike times from the other ear having the appropriate difference in *starting-phase*. While maintaining the proper *start-IPD*, each AMBB period histogram pooled spikes resulting from stimuli using the 8 *starting-phases* spanning each carrier period. Thus whilst the histograms show the effects of *start-IPD*, they do not show phase-locking to fine structure of the carriers.

In this study, “best-ITD during rise” denotes *start-IPD* = 270°; “best-ITD at peak” denotes *start-IPD* = 180°; and “best-ITD during fall” denotes *start-IPD* = 90°.

Chi-squared tests for significant differences in model spike counts

For each condition and modulation frequency, a chi-squared test for one and two degrees of freedom (2-way and 3-way comparisons) compared spike counts from the nonlinear model MSO neuron stimulated with AMBBs with best-ITD occurring during rising vs. peak vs. falling amplitude. Each chi-squared test yielded a probability (p) of the null hypothesis that the differences in spike count occurred randomly.

Synchrony index and Rayleigh statistic for significant phase-locking:

For each modulation frequency and *starting-phase* combination, the synchrony index (*SI, R*) of spike times (t_i) (70) with respect to their phase θ_i within the AM cycle (with modulation frequency f_m and modulation period $T_m = 1/f_m$) was calculated:

$$\theta_i \triangleq 2\pi f_m mod(t_i, T_m)$$

$$SI = \sqrt{(\sum_{i=1}^{N} \cos\theta_i\,)^2 + (\sum_{i=1}^{N} \sin\theta_i\,)^2}$$, where N is the spike count.

The Rayleigh significance statistic ($2NR^2$) was then calculated and converted to a *p* value, the probability of the null hypothesis that the AM period-histogram of spike times resulted from a uniform distribution (71):

p	0.10	0.05	0.025	0.01	0.001
$2NR^2$	4.605	5.991	7.378	9.210	13.816

Lateralisation model including linear-membrane models

To study how synaptic adaptation and biophysical profiles could impact lateralisation of acoustic stimuli in anechoic and reverberant conditions, we constructed a model of lateralisation whose brainstem stages (SBCs and MSO neurons) are represented by point neurons with linear biophysical properties (20). Two stimuli were presented to the model: the first, a SAM tone with non-zero ITDs inserted at different phases of the AM cycle, as used behaviourally to determine how carrier frequency affects ITD sensitivity over the time course of an AM cycle (9); the second, a natural speech stimulus with early reflections, has been proposed as a simple simulation of a reverberant environment where correct lateralisation is only possible if ITD cues in the onset waveform are processed preferentially (4).

SAM tones with non-zero ITDs inserted at different phases of AM cycle

This stimulus was generated according to the Hu et al. study (9) that first used it. In summary, SAM tones were created from pulse trains that had been bandpass-filtered and then amplitude-modulated. Non-stationary ITDs were added by temporally shifting individual pulses in one of either the rising, peak or falling phases of the AM cycle. For the purposes of this study, non-stationary ITDs of +300 μs and +150 μs were inserted into SAM tones of either 200-Hz or 600-Hz carrier frequency respectively. These ITD values were chosen based on individual behavioural thresholds in the Hu et al. study (9). At each carrier frequency, four conditions were tested: two different AM frequencies (8 Hz or 20 Hz) and two different proportions of rising, peak or falling AM phases with a non-zero ITD inserted (20% or 40%). These parameters match those tested behaviourally by (9).

A natural speech stimulus with early reflections

A single monosyllabic consonant-vowel nucleus-consonant (CNC) word token, ‘church’, (spoken by an Australian-English, female voice), was selected as a stimulus (Fig. 1 and Fig. 8). To simulate its arrival from a location one metre away to the right of the midline in an anechoic environment, the word’s waveform (normalised at 70dB) was convolved with a large pinnae HRTF for +30° azimuthal location (CIPIC database, UC Davis). A reverberant space was simulated by adding to the direct (+30°) pathway two early reflections off virtual walls stood behind and to the right of the subject (Fig. 1). These reflected copies of the words arrived from -65° and -130° angles (again convolved with large-pinnae HRTFs from the CIPIC database) and were delayed by 4ms and 8ms respectively to reproduce their elongated paths (4).

Linear model circuitry

The linear model, like its nonlinear counterpart, consists of three stages: an initial auditory periphery stage (the middle/inner ear and auditory nerve fibres) and two brainstem stages (cochlear nuclei and MSO). Unlike the nonlinear model however, the linear model incorporates two parallel circuits, representing the ‘left’ and ‘right’ MSO nuclei and their inputs. The difference in output rate between these parallel circuits is utilised to calculate lateralisation of the natural stimulus. The only discernible difference between ‘left’ and ‘right’ circuits is the contralateral $\frac{1}{8}$ pi shifts in their MSO neurons’ IPD tuning curve peaks which are generated by delaying the outputs from the auditory periphery stage ipsilateral to the MSO nucleus in question. This shift is considered physiological given experimentally observed binaural tuning curves from the auditory brainstem whose optimal characteristics have been corroborated theoretically (34).

Auditory periphery stage

Peripheral processing of the acoustic stimuli in the linear model is performed using an implementation of the Zilany et al. (21) cat middle/inner ear model in Matlab. Outputs from the auditory periphery are restricted to 200-Hz/ 600-Hz for the pulse-shifted SAM tones (matching their SAM tone’s carrier frequency) and 600-Hz for lateralisation of the speech stimulus with early reflections. This latter value was chosen based on it laying in the middle of the 500-750 Hz frequency range in which TFS-ITD sensitivity is considered strongest (37). When exploring effects, of synaptic depression at the inputs from auditory nerve to cochlear nucleus, on the lateralisation of a speech stimulus, the same auditory periphery simulations are used for both the depressing and non-depressing inputs to the cochlear nuclei.

Linear-membrane model properties

Single-compartment, linear-membrane models are used to represent both SBC and MSO neurons in the linear model. These linear-membrane models can incorporate two dynamic currents as previously described in (20): I_w, a resonant current and/or, I_n, an amplifying current. The current balance equation for the general neural model is as follows:

$$\mathrm{c}\frac{dv}{dt} = -g_{\mathrm{M}}v - g_{\mathrm{w}}w_{\mathrm{w}} + g_{\mathrm{n}}w_{\mathrm{n}} + \mathrm{I}_{app}(t)$$

Where c is capacitance (picofarads), g_M is total membrane conductance (nanosiemens) and I_{app} is the current (picoampere) applied to the neural model. The resonant and amplifying currents, I_w and I_n, are described by their conductances, g_W and g_n (in nanosiemens); the dynamics of their gating variables, w_w and w_n (in millivolts) are described generically by the equation:

$$\tau_{\mathrm{w}}\frac{dw_{\mathrm{w}}}{dt} = v - w_w$$

$$\tau_{\mathrm{w}}\frac{dw_{\mathrm{w}}}{dt} = v - w_w$$

Where w_x is the gating variable whose associated time constant is τ_x (milliseconds).

Two parameter sets are chosen to represent the apparent bimodality of subthreshold biophysical properties in the gerbil MSO *in vitro* (30). These example models can be broadly characterised by their impedance profiles as either band-pass with a high resonant-frequency or band-pass with a low resonant-frequency (20). While the band-pass model with a high-resonant frequency is exclusively chosen to represent SBCs, both model types are used to represent MSO neurons.

825 *Synaptic properties and adaptation*

826 As in the nonlinear model, 3 independently-simulated auditory nerve fibres provide excitatory
827 drive to each SBC in the linear model. Excitatory unitary conductances at this synapse are
828 modelled as alpha functions with an exponential time course of 0.2ms. Synaptic depression
829 with a single exponential recovery is also implemented at this stage, matching the adaptation
830 observed in the nonlinear model functionally thanks to its similar parameters (u = 0.55; τ = 25
831 ms).

832 Each MSO neuron receives 4 (independently-simulated) excitatory cochlear-nucleus inputs
833 from "either ear" in the linear model. Alpha functions are again used to model the unitary
834 excitatory conductances at this synapse with time courses selected relative to the resonant
835 class of the MSO in question (i.e. band-pass with high resonant-frequency: 0.2ms; band-pass
836 with low resonant-frequency: 0.5ms). This increase in synaptic time course is performed to
837 reflect the slower membrane time constant associated with neurons displaying little or no
838 resonance at all. If, as expected, MSO neurons with slower intrinsic properties still segregate
839 inputs from either ear on either dendrite then the increased electrotonic propagation of
840 excitatory inputs somatopetally should lead to slower excitatory potentials at their somata.
841 Where comparisons of the two MSO resonant classes are made, the same adapting auditory
842 nerve inputs are presented to their respective cochlear-nucleus stages, therefore reducing any
843 potential confusion that might result from variability in the peripheral model's output.

844 *Spike thresholds in the linear-membrane model*

845 Idealised thresholds for the linear-membrane model are implemented from Remme et al. (20).
846 A slope threshold (dv/dt) is used for all neuronal types. Threshold values for cochlear-nucleus
847 cells are selected to produce good average firing rate without undermining the effects of

synaptic depression. Threshold values for the MSO neurons are selected to obtain maximum dynamic range of ITD tuning functions for 200/600 Hz pure tone stimuli (where dynamic range is considered the difference between the maximum and minimum ITD-modulated spike rate). A refractory period of 1 ms is implemented as in Remme et al. (20) for cochlear-nucleus neurons and MSO neurons with a high-resonant frequency whereas a longer refractory period of 2 ms is used for the MSO neurons with low-resonant frequency, reflecting longer refractory periods in neurons with lower densities of K_{LT} channels (19,26,72).

Calculating lateralisation using d' values

Lateralisation of a reverberant natural stimulus is judged in the linear model by calculating the mean spike rate difference between a population of 50 'left' and 50 'right' MSO neurons to a single stimulus presentation. d' values are calculated to quantify the degree of separation of 'left' and 'right' spike rates using the following equation:

$$d' = \frac{\mu_L - \mu_R}{\sqrt{\frac{1}{2}(\sigma_L^2 + \sigma_R^2)}}$$

Where μ_L is the mean spike rate for the 'left' population of MSO neurons in 5-ms bins; μ_R is the mean spike rate for the 'right' population of MSO neurons in 5-ms bins; σ_L is the standard deviation of the 'left' MSO population's spike rate and σ_R is the standard deviation of the 'right' population's spike rate (both calculated in 5-ms bins again).

The sign and magnitude of the d' allows judgement of whether the linear model lateralises the reverberant stimulus to the correct direction (negative d' values denote negative ITDs/left of midline; positive d' values denote positive ITDs/right of midline) and whether this lateralisation

judgment is considered significant (d’ > 1 or d’ < -1 indicated a significant lateralisation in the right and left directions respectively).

ANOVA and T-test for significant differences in lateralisation

Two-way and three-way ANOVAs are implemented to compare the duration of correct lateralisations (time correctly lateralised = bin duration x number of bins where d’ > 1) by the hemispheric model of SAM tones with non-zero ITDs in either the rising, peak or falling phases as well as the percentage of the phase including a non-zero ITD. A two-tailed T-test is also performed for 200-Hz carrier SAM tones to compare the effect of MSO neuronal type. For the speech stimulus, a paired two-tailed T-test is performed to compare the frequency of incorrect lateralisations (time incorrectly lateralised = bin duration x number of bins where d’ <-1) in the linear model with either adapting or non-adapting auditory nerve inputs.

Acknowledgements

Funding

This work was supported by Australian Research Council Laureate Fellowship (FL160100108) awarded to DM

Author Contributions

AB and JMH contributed equally.

Conceptualisation: DM and MD

Data Curation: JMH and AB

Formal Analysis: JMH and AB

Funding Acquisition: DM

Investigation: AB and JMH

Methodology: AB (nonlinear modelling) and JMH (linear modelling)

Resources: DM, AB, and JMH

Software: AB and JMH

Supervision: DM

Visualization: JMH and AB

Validation: AB and JMH

Writing – Original Draft Preparation: AB, JMH, and DM

Writing – Review & Editing: AB, DM, MD, and JMH

References

1. Cherry EC. Some experiments on the recognition of speech, with one and with 2 ears. JASA. 1953;(25):975–9.

2. Dietz M, Marquardt T, Salminen NH, McAlpine D. Emphasis of spatial cues in the temporal fine structure during the rising segments of amplitude-modulated sounds. Proc Natl Acad Sci [Internet]. 2013;110(37):15151–15156. Available from: www.pnas.org/cgi/doi/10.1073/pnas.1309712110

3. Haas H. The influence of a single echo on the audibility of speech. Acoustica. 1951;1:49–58.

4. Dietz M, Marquardt T, Stange A, Pecka M, Grothe B, McAlpine D. Emphasis of spatial cues in the temporal fine structure during the rising segments of amplitude-modulated sounds II: single-neuron recordings. J Neurophysiol [Internet]. 2014;111(10):1973–85. Available from: http://jn.physiology.org/cgi/doi/10.1152/jn.00681.2013

5. Fitzpatrick DC, Kuwada S, Kim DO, Parham K, Batra R. Responses of neurons to click-pairs as simulated echoes: Auditory nerve to auditory cortex. J Acoust Soc Am. 1999;106(6):3460–72.

6. Liebenthal E, Pratt H. Human auditory cortex electrophysiological correlates of the precedence effect: Binaural echo lateralization suppression. J Acoust Soc Am. 2002;106(1):291–303.

7. Litovsky RY, Yin TC. Physiological studies of the precedence effect in the inferior colliculus of the cat. I. Correlates of psychophysics. J Neurophysiol [Internet]. 1998;80(3):1285–301. Available from: https://doi.org/10.1152/jn.1998.80.3.1285

8. Litovsky RY, Yin TCT. Physiological Studies of the Precedence Effect in the Inferior Colliculus of the Cat. II. Neural Mechanisms. J Neurophysiol. 1998;80(3):1302–16.

9. Hu H, Ewert SD, McAlpine D, Dietz M. Differences in the temporal course of interaural time difference sensitivity between acoustic and electric hearing in amplitude modulated stimuli. J

920 Acoust Soc Am [Internet]. 2017;141(3):1862–73. Available from:
921 http://aip.scitation.org/doi/10.1121/1.4977014

922 10. Traer J, McDermott JH. Statistics of natural reverberation enable perceptual separation of sound
923 and space. Proc Natl Acad Sci [Internet]. 2016;113(48):E7856–65. Available from:
924 http://www.pnas.org/lookup/doi/10.1073/pnas.1612524113

925 11. Oleskevich S, Clements J, Walmsley B. Release probability modulates short-term plasticity at a
926 rat giant terminal. J Physiol. 2000;524(2):513–23.

927 12. Wang Y, Manis PB. Short-Term Synaptic Depression and Recovery at the Mature Mammalian
928 Endbulb of Held Synapse in Mice. J Neurophysiol [Internet]. 2008;100(3):1255–64. Available from:
929 http://jn.physiology.org/cgi/doi/10.1152/jn.90715.2008%5Cnpapers2://publication/doi/10.1152/jn.
930 90715.2008

931 13. Yang H, Xu-Friedman MA. Impact of Synaptic Depression on Spike Timing at the Endbulb of Held.
932 J Neurophysiol [Internet]. 2009;102(3):1699–710. Available from:
933 http://jn.physiology.org/cgi/doi/10.1152/jn.00072.2009

934 14. Yang H, Xu-Friedman MA. Skipped-Stimulus Approach Reveals That Short-Term Plasticity
935 Dominates Synaptic Strength during Ongoing Activity. J Neurosci [Internet]. 2015;35(21):8297–
936 307. Available from: http://www.jneurosci.org/cgi/doi/10.1523/JNEUROSCI.4299-14.2015

937 15. Mathews PJ, Jercog PE, Rinzel J, Scott LL, Golding NL. Control of submillisecond synaptic timing
938 in binaural coincidence detectors by K v 1 channels. Nat Neurosci [Internet]. 2010;13(5):601–9.
939 Available from: http://dx.doi.org/10.1038/nn.2530

940 16. Gai Y, Doiron B, Kotak V, Rinzel J. Noise-Gated Encoding of Slow Inputs by Auditory Brain Stem
941 Neurons With a Low-Threshold K+ Current. J Neurophysiol [Internet]. 2009;102(6):3447–60.
942 Available from: http://jn.physiology.org/cgi/doi/10.1152/jn.00538.2009

943 17. Svirskis G, Kotak V, Sanes D, Rinzel J. Sodium Along With Low-Threshold Potassium Currents
944 Enhance Coincidence Detection of Subthreshold Noisy Signals in MSO Neurons. J Neurophysiol
945 [Internet]. 2004;91(6):2465–73. Available from:
946 http://jn.physiology.org/cgi/doi/10.1152/jn.00717.2003

947 18. Svirskis G, Kotak V, Sanes D, Rinzel J. Enhancement of signal-to-noise ratio and phase locking
948 for small inputs by a low-threshold outward current in auditory neurons. J Neurosci.
949 2002;22(24):11019–25.

950 19. Rothman JS, Manis PB. Differential Expression of Three Distinct Potassium Currents in the Ventral
951 Cochlear Nucleus. J Neurophysiol [Internet]. 2003;89(6):3070–82. Available from:
952 http://www.physiology.org/doi/10.1152/jn.00125.2002

953 20. Remme MWH, Donato R, Mikiel-Hunter J, Ballestero JA, Foster S, Rinzel J, et al. Subthreshold
954 resonance properties contribute to the efficient coding of auditory spatial cues. Proc Natl Acad Sci
955 [Internet]. 2014;111(22):E2339–48. Available from:
956 http://www.pnas.org/cgi/doi/10.1073/pnas.1316216111

957 21. Zilany MSA, Bruce IC, Carney LH. Updated parameters and expanded simulation options for a
958 model of the auditory periphery. J Acoust Soc Am [Internet]. 2014;135(1):283–6. Available from:
959 http://asa.scitation.org/doi/10.1121/1.4837815

960 22. Glasberg BR, Moore BCJ. Derivation of auditory filter shapes from notched-noise data. Hear Res.
961 1990;47:103–38.

962 23. Rudnicki M, Hemmert W. High Entrainment Constrains Synaptic Depression Levels of an In vivo
963 Globular Bushy Cell Model. Front Comput Neurosci [Internet]. 2017;11(March):1–11. Available
964 from: http://journal.frontiersin.org/article/10.3389/fncom.2017.00016/full

965 24. Hodgkin AL, Huxley AF. A quantitative description of ion currents and its applications to conduction

and excitation in nerve membranes. J Physiol. 1952;117:500–44.

25. Mathews PJ, Jercog PE, Rinzel J, Scott LL, Golding NL. Control of submillisecond synaptic timing in binaural coincidence detectors by K v 1 channels. Nat Neurosci. 2010;13(5):601–9.

26. Rothman JS, Manis PB. The Roles Potassium Currents Play in Regulating the Electrical Activity of Ventral Cochlear Nucleus Neurons. J Neurophysiol [Internet]. 2003;89(6):3097–113. Available from: https://www.physiology.org/doi/full/10.1152/jn.00127.2002

27. Scott LL, Mathews PJ, Golding NL. Perisomatic Voltage-Gated Sodium Channels Actively Maintain Linear Synaptic Integration in Principal Neurons of the Medial Superior Olive. J Neurosci [Internet]. 2010;30(6):2039–50. Available from: http://www.jneurosci.org/cgi/doi/10.1523/JNEUROSCI.2385-09.2010

28. Joris PX, Smith PH, Yin TC, Carney LH. Enhancement of neural synchronization in the anteroventral cochlear nucleus. II. Responses in the tuning curve tail. J Neurophysiol. 1994;

29. Yin CT, Chan JCM. Interaural time sensitivity in medial superior olive of cat. J Neurophysiol. 1990;64(2):465–88.

30. Bondy B, Golding NL. Variations in intrinsic and synaptic properties in MSO neurons confer a spectrum of ITD sensitivity. ARO midwinter Meet San Diego, CA, USA. 2018;

31. Colburn HS, Chung Y, Zhou Y, Brughera A. Models of brainstem responses to bilateral electrical stimulation. JARO - J Assoc Res Otolaryngol. 2009;10(1):91–110.

32. Chung Y, Delgutte B, Colburn HS. Modeling Binaural Responses in the Auditory Brainstem to Electric Stimulation of the Auditory Nerve. JARO - J Assoc Res Otolaryngol. 2015;16(1):135–58.

33. Dietz M, Ewert SD, Hohmann V. Model-based direction estimation of concurrent speakers in the horizontal plane. J Acoust Soc Am. 2009;125(4):2527.

988 34. McAlpine D, Jiang D, Palmer AR. A neural code for low-frequency sound localization in mammals.
989 Nat Neurosci. 2001;4(4):396–401.

990 35. Devore S, Ihlefeld A, Hancock K, Shinn-Cunningham B, Delgutte B. Accurate Sound Localization
991 in Reverberant Environments Is Mediated by Robust Encoding of Spatial Cues in the Auditory
992 Midbrain. Neuron [Internet]. 2009;62(1):123–34. Available from:
993 http://dx.doi.org/10.1016/j.neuron.2009.02.018

994 36. Brughera A, Dunai L, Hartmann WM. Human interaural time difference thresholds for sine tones:
995 The high-frequency limit. J Acoust Soc Am [Internet]. 2013;133(5):2839–55. Available from:
996 http://asa.scitation.org/doi/10.1121/1.4795778

997 37. Ihlefeld A, Shinn-Cunningham BG. Effect of source spectrum on sound localization in an everyday
998 reverberant room. J Acoust Soc Am. 2011;130(1):324–33.

999 38. Klumpp RG, Eady HR. Some Measurements of Interaural Time Difference Thresholds. J Acoust
1000 Soc Am [Internet]. 1956;28(5):859–60. Available from:
1001 http://asa.scitation.org/doi/10.1121/1.1908493

1002 39. Shinn-Cunningham BG, Zurek PM, Durlach NI, Clifton RK. Cross-frequency interactions in the
1003 precedence effect. J Acoust Soc Am. 1995;98(1):164–71.

1004 40. Xia J, Brughera A, Colburn HS, Shinn-Cunningham B. Physiological and psychophysical modeling
1005 of the precedence effect. JARO - J Assoc Res Otolaryngol. 2010;11(3):495–513.

1006 41. Kuenzel T, Borst JGG, van der Heijden M. Factors Controlling the Input-Output Relationship of
1007 Spherical Bushy Cells in the Gerbil Cochlear Nucleus. J Neurosci [Internet]. 2011;31(11):4260–
1008 73. Available from: http://www.jneurosci.org/cgi/doi/10.1523/JNEUROSCI.5433-10.2011

1009 42. Young ED, Sachs MB. Auditory nerve inputs to cochlear nucleus neurons studied with cross-
1010 correlation. Neuroscience. 2008;154(1):127–38.

1011 43. Smith PH, Joris PX, Yin TCT. Projections of physiologically characterized spherical bushy cell
1012 axons from the cochlear nucleus of the cat: Evidence for delay lines to the medial superior olive.
1013 J Comp Neurol. 1993;331(2):245–60.

1014 44. Roberts MT, Seeman SC, Golding NL. A mechanistic understanding of the role of feedforward
1015 inhibition in the mammalian sound localization circuitry. Neuron [Internet]. 2013;78(5):923–35.
1016 Available from: http://dx.doi.org/10.1016/j.neuron.2013.04.022

1017 45. Fischl MJ, Combs TD, Klug A, Grothe B, Burger RM. Modulation of synaptic input by GABAB
1018 receptors improves coincidence detection for computation of sound location. J Physiol.
1019 2012;590(13):3047–66.

1020 46. Brand A, Behrend O, Marquardt T, McAlpine D, Grothe B. Precise inhibition is essential for
1021 microsecond interaural time difference coding. Nature. 2002;417(6888):543–7.

1022 47. Grothe B. New roles for synaptic inhibition in sound localization. Nat Rev Neurosci. 2003;4(7):540–
1023 50.

1024 48. Bradley JS, Sato H, Picard M. On the importance of early reflections for speech in rooms. J Acoust
1025 Soc Am. 2003;113(6):3233.

1026 49. Gourévitch B, Brette R. The impact of early reflections on binaural cues. J Acoust Soc Am.
1027 2012;132(1):9–27.

1028 50. Wallach H, Newman EB, Rosenzweig MR. The precedence effect in sound localization. Am J
1029 Psychol. 1949;62(3):315–336.

1030 51. Brown AD, Jones HG, Kan A, Thakkar T, Stecker GC, Goupell MJ, et al. Evidence for a neural
1031 source of the precedence effect in sound localization. J Neurophysiol. 2015;114(5):2991–3001.

1032 52. Burger RM, Pollak GD. Reversible Inactivation of the Dorsal Nucleus of the Lateral Lemniscus
1033 Reveals Its Role in the Processing of Multiple Sound Sources in the Inferior Colliculus of Bats. J

1034 Neurosci. 2001;21(13):4830–43.

1035 53. Kidd SA, Kelly JB. Contribution of the Dorsal Nucleus of the Lateral Lemniscus to Binaural
1036 Responses in the Inferior Colliculus of the Rat: Interaural Time Delays. J Neurosci.
1037 1996;16(22):7390–7.

1038 54. Pecka M, Zahn TP, Saunier-Rebori B, Siveke I, Felmy F, Wiegrebe L, et al. Inhibiting the Inhibition:
1039 A Neuronal Network for Sound Localization in Reverberant Environments. J Neurosci [Internet].
1040 2007;27(7):1782–90. Available from: http://www.jneurosci.org/cgi/doi/10.1523/JNEUROSCI.5335-
1041 06.2007

1042 55. Keine C, Rubsamen R, Englitz B. Signal integration at spherical bushy cells enhances
1043 representation of temporal structure but limits its range. Elife. 2017;6:1–16.

1044 56. Adams JC, Mugnaini E. Immunocytochemical evidence for inhibitory and disinhibitory circuits in
1045 the superior olive. Hear Res. 1990;49(1–3):281–98.

1046 57. Cant NB, Hyson RL. Projections from the lateral nucleus of the trapezoid body to the medial
1047 superior olivary nucleus in the gerbil. Hear Res. 1992;58(1):26–34.

1048 58. Smith PH, Joris PX, Carney LH, Yin TCT. Projections of physiologically characterized globular
1049 bushy cell axons from the cochlear nucleus of the cat. J Comp Neurol. 1991;304(3):387–407.

1050 59. Srinivasan S, Laback B, Majdak P, Delgutte B. Introducing Short Interpulse Intervals in High-Rate
1051 Pulse Trains Enhances Binaural Timing Sensitivity in Electric Hearing. JARO - J Assoc Res
1052 Otolaryngol. 2018;19(3):301–15.

1053 60. Hancock KE, Chung Y, Delgutte B. Neural ITD coding with bilateral cochlear implants: effect of
1054 binaurally coherent jitter. J Neurophysiol [Internet]. 2012;108(3):714–28. Available from:
1055 http://jn.physiology.org/cgi/doi/10.1152/jn.00269.2012

1056 61. Smith ZM, Delgutte B. Sensitivity to Interaural Time Differences in the Inferior Colliculus with

1057 Bilateral Cochlear Implants. J Neurosci [Internet]. 2007;27(25):6740–50. Available from:
1058 http://www.jneurosci.org/cgi/doi/10.1523/JNEUROSCI.0052-07.2007

1059 62. Stimberg M, Goodman D, Benichoux V, Brette R. Brian 2-the second coming: spiking neural
1060 network simulation in Python with code generation. Bmc … [Internet]. 2013;14(Suppl 1):P38.
1061 Available from: http://www.biomedcentral.com/1471-2202/14/S1/P38

1062 63. Joris PX, Yin TCT. Responses to amplitude-modulated tones in the auditory nerve of the cat. J
1063 Acoust Soc Am. 1992;91:215–32.

1064 64. Rhode WS, Greenberg S. Encoding of amplitude modulation in the cochlear nucleus of the cat. J
1065 Neurophysiol. 1994;

1066 65. Lorente De No R. The Primary Acoustic Nuclei. New York: Raven; 1981.

1067 66. Couchman K, Grothe B, Felmy F. Medial Superior Olivary Neurons Receive Surprisingly Few
1068 Excitatory and Inhibitory Inputs with Balanced Strength and Short-Term Dynamics. J Neurosci
1069 [Internet]. 2010;30(50):17111–21. Available from:
1070 http://www.jneurosci.org/cgi/doi/10.1523/JNEUROSCI.1760-10.2010

1071 67. Zhou Y, Carney LH, Colburn HS. A Model for Interaural Time Difference Sensitivity in the Medial
1072 Superior Olive: Interaction of Excitatory and Inhibitory Synaptic Inputs, Channel Dynamics, and
1073 Cellular Morphology. J Neurosci [Internet]. 2005;25(12):3046–58. Available from:
1074 http://www.jneurosci.org/cgi/doi/10.1523/JNEUROSCI.3064-04.2005

1075 68. Mikiel-Hunter J, Kotak V, Rinzel J. High-Frequency Resonance in the Gerbil Medial Superior Olive.
1076 PLoS Comput Biol [Internet]. 2016;12(11):1–23. Available from:
1077 http://dx.doi.org/10.1371/journal.pcbi.1005166

1078 69. Scott LL, Hage TA, Golding NL. Weak action potential backpropagation is associated with high-
1079 frequency axonal firing capability in principal neurons of the gerbil medial superior olive. J Physiol.

1080 2007;583(2):647–61.

1081 70. Johnson DH. The relationship between spike rate and synchrony in responses of auditory-nerve
1082 fibers to single tones. J Acoust Soc Am. 1980;68:1115–22.

1083 71. Rhode WS. A test for the significance of the mean direction and the concentration parameter of a
1084 circular distribution. Madison Univ Wisconsin Dept Neurophysiol Report [Internet]. 1976; Available
1085 from: http://www.neurophys.wisc.edu/comp/docs/not011/not011.html

1086 72. Rothman JS, Manis PB. Kinetic Analyses of Three Distinct Potassium Conductances in Ventral
1087 Cochlear Nucleus Neurons. J Neurophysiol [Internet]. 2003;89(6):3083–96. Available from:
1088 http://www.physiology.org/doi/10.1152/jn.00126.2002

1089

Figures

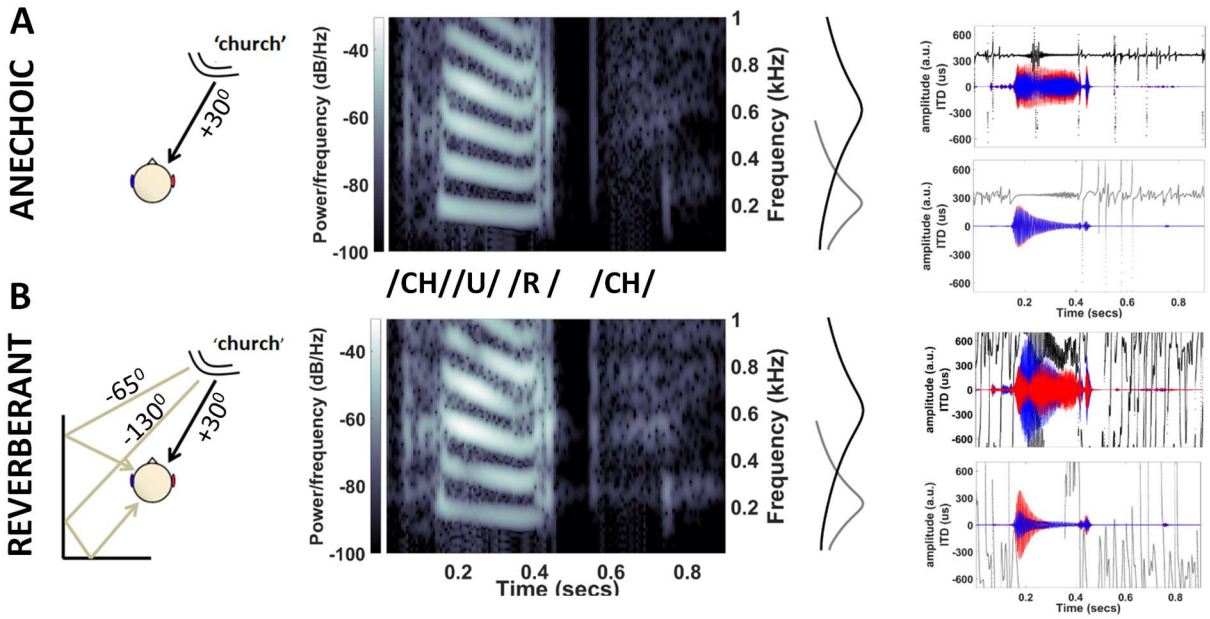

Figure 1 [in colour, online and in print]

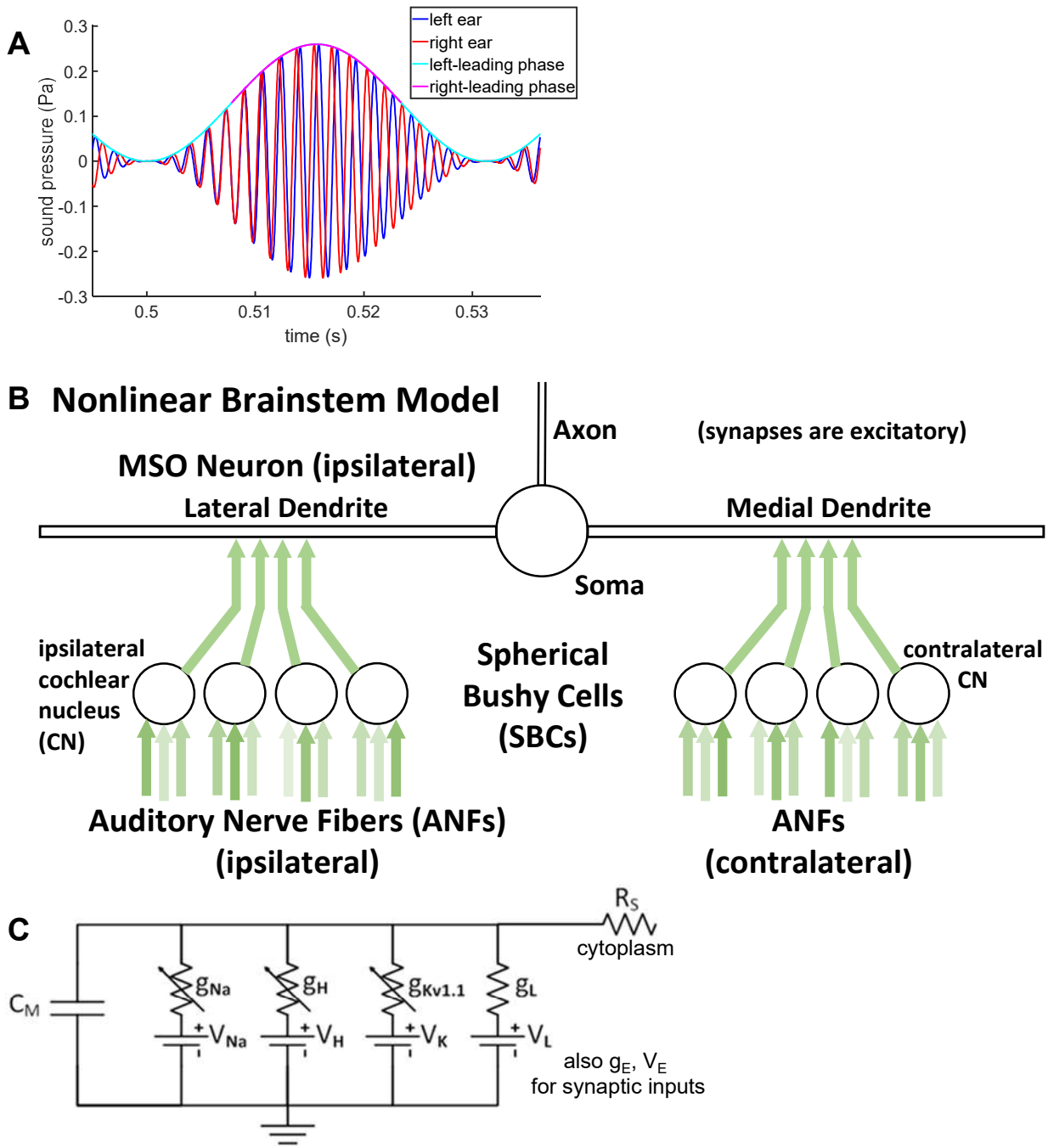

Figure 2 [in colour, online and in print]

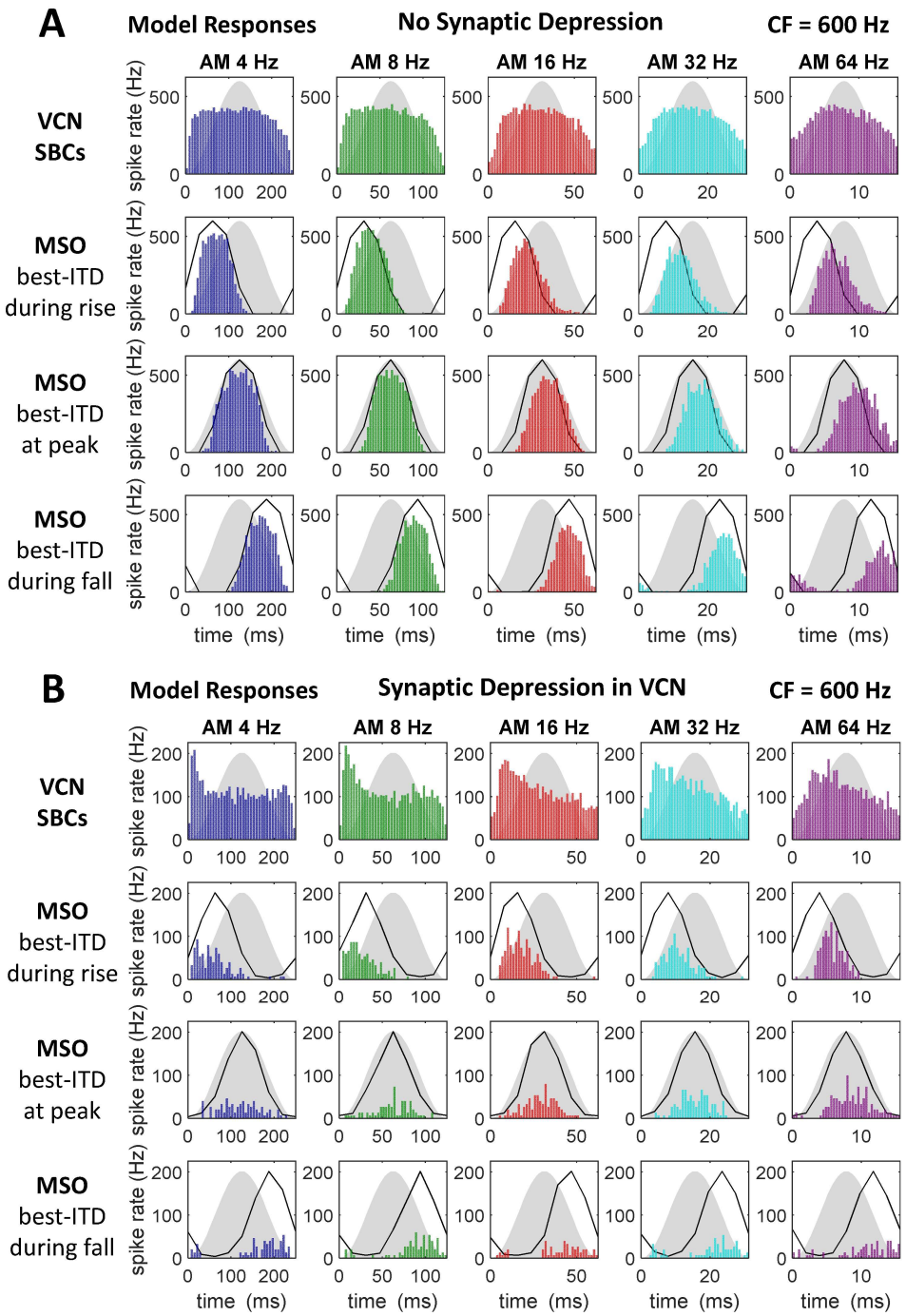

Figure 3 [in colour, online and in print]

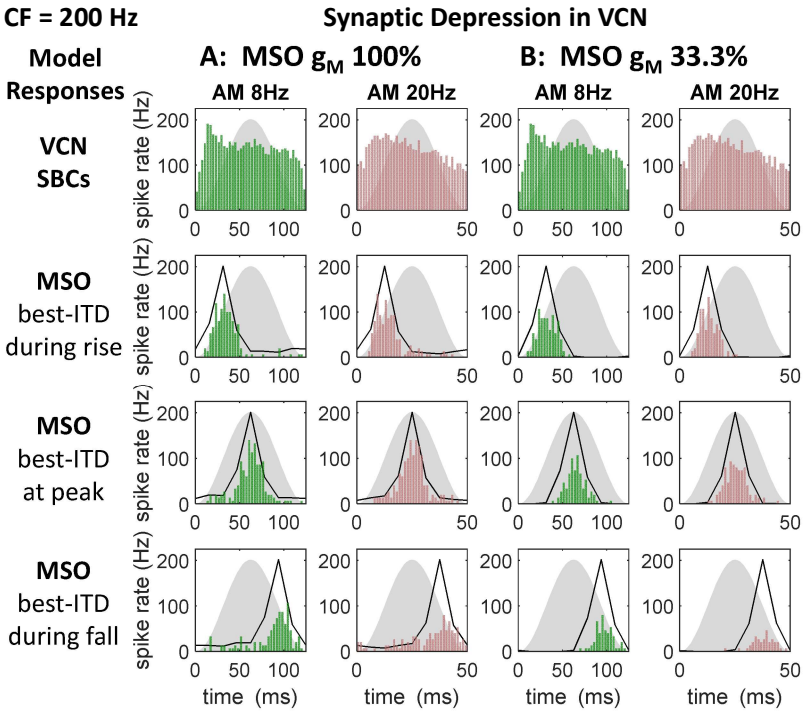

Figure 4 [in colour, online and in print]

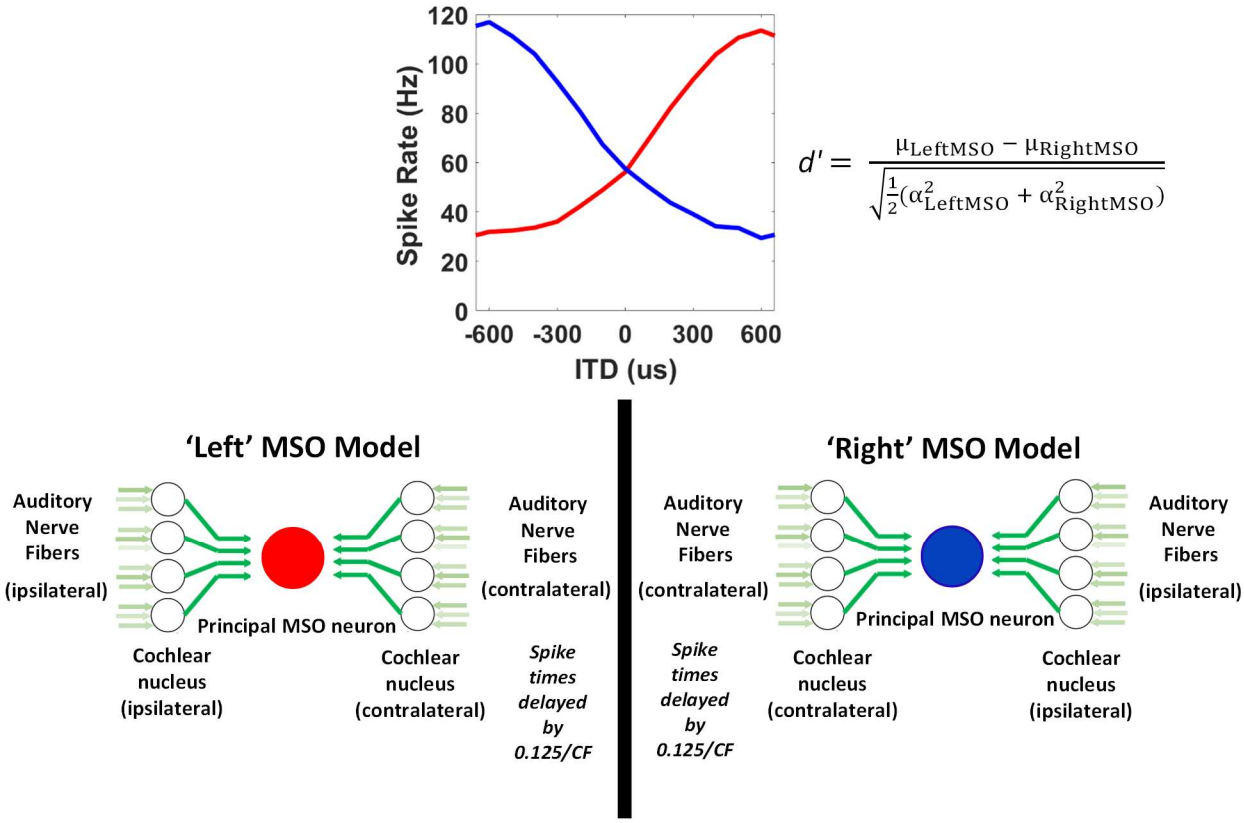

Figure 5 [in colour, online and in print]

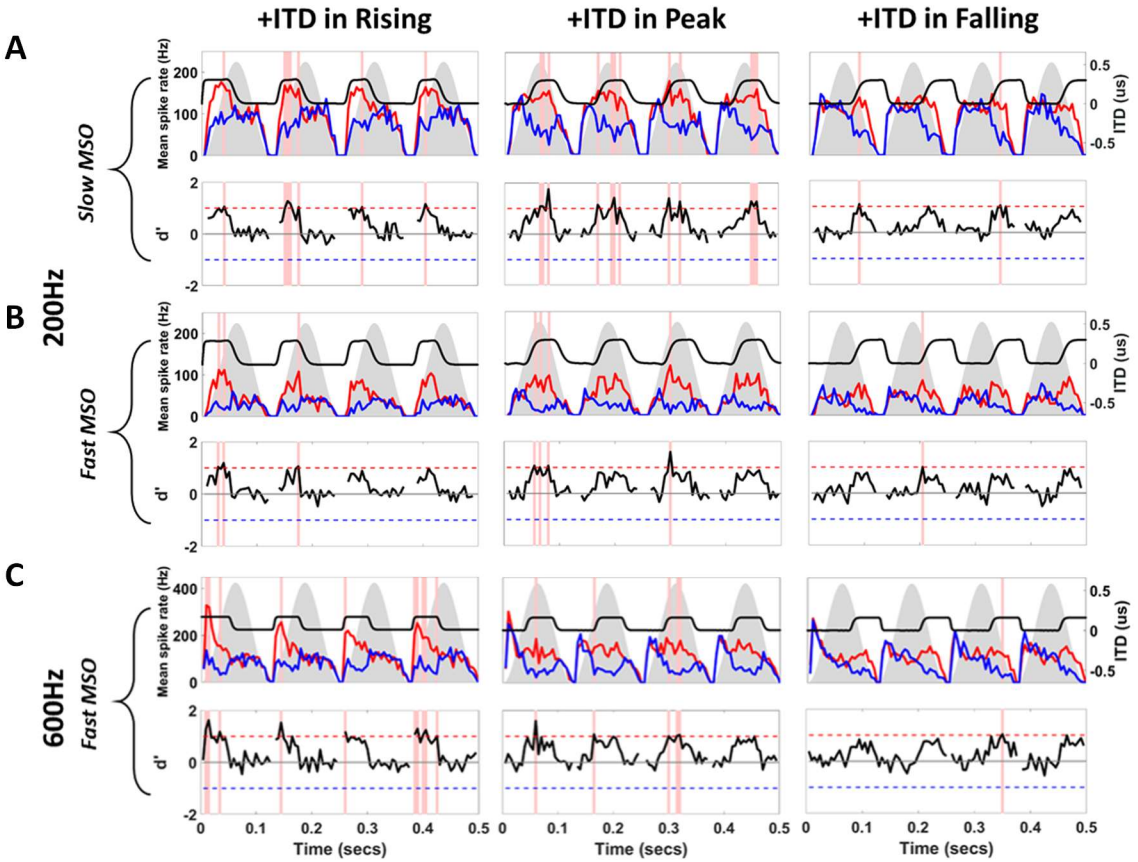

Figure 6 [in colour, online and in print]

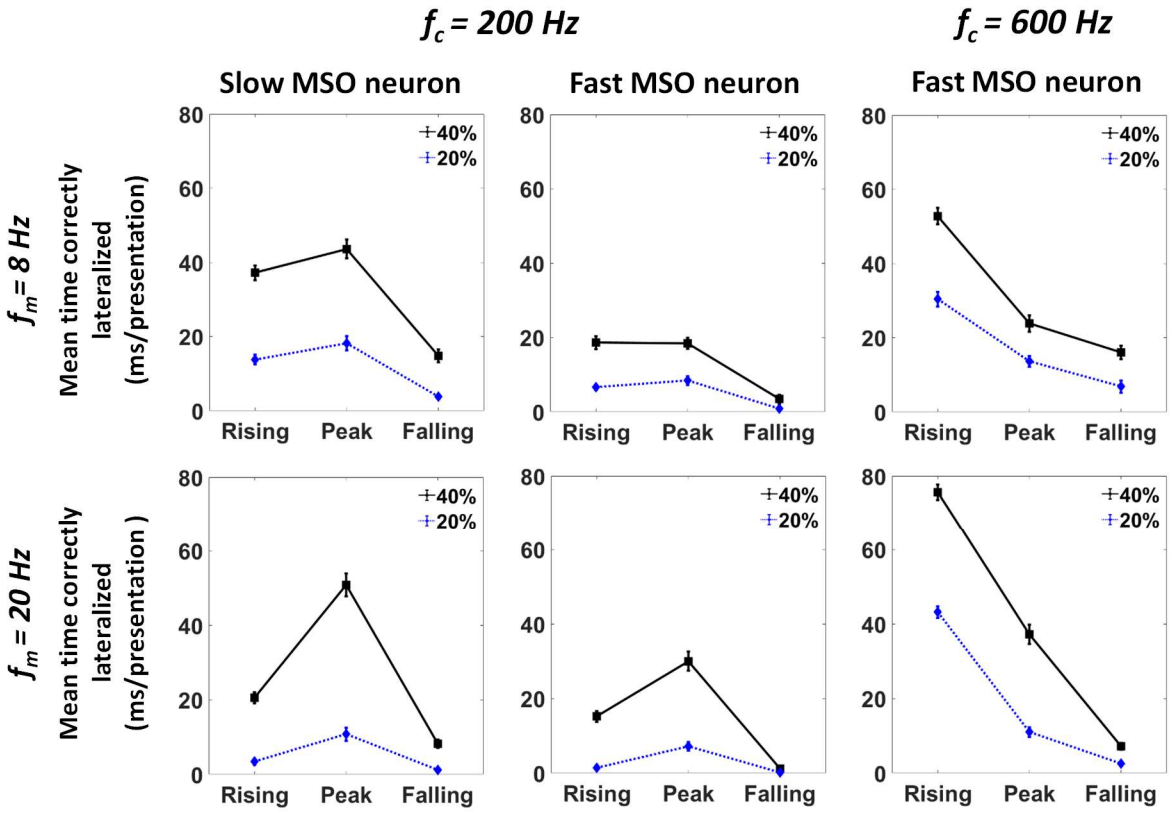

1116

1117

1118 **Figure 7 [in colour, online and in print]**

1119

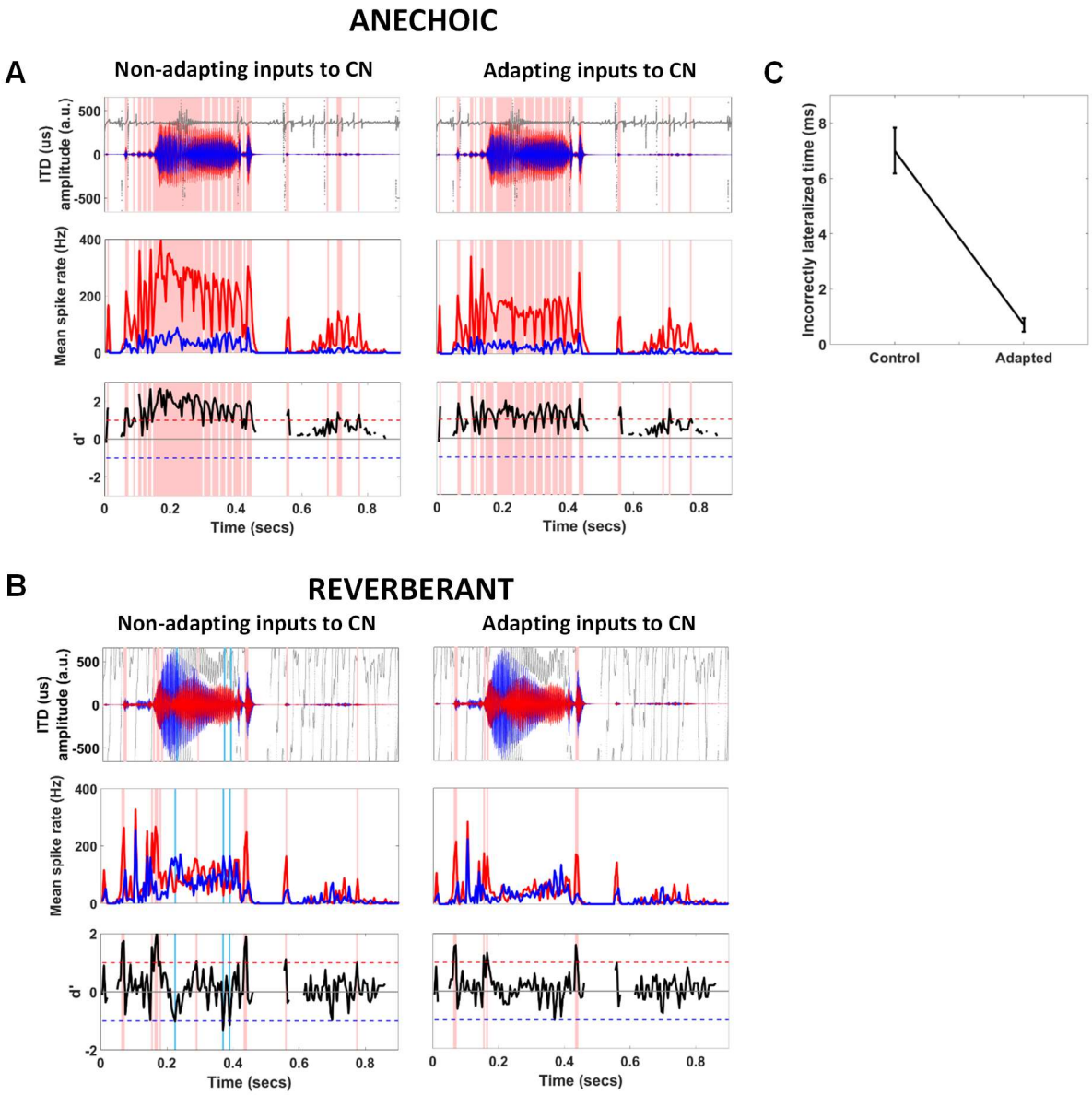

Figure 8 [in colour, online and in print]